



STUDY OF THE REPRESENTATIVE ELEMENTARY VOLUME OF CARBONATE
ROCKS AND PORE NETWORK SIMULATION

Marianna Dantas da Silva

Dissertação de Mestrado apresentada ao Programa de Pós-graduação em Engenharia Civil, COPPE, da Universidade Federal do Rio de Janeiro, como parte dos requisitos necessários à obtenção do título de Mestre em Engenharia Civil

Orientador: Paulo Couto

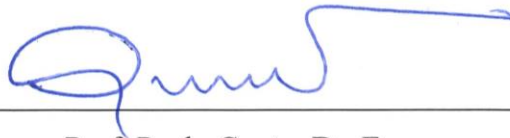
Rio de Janeiro
Setembro de 2019

STUDY OF THE REPRESENTATIVE ELEMENTARY VOLUME OF CARBONATE
ROCKS AND PORE NETWORK SIMULATION

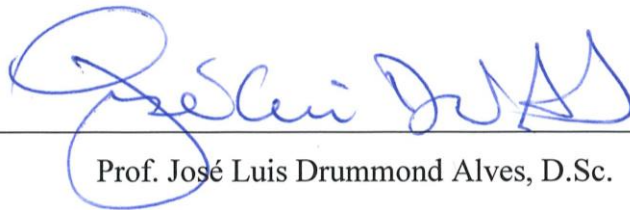
Marianna Dantas da Silva

DISSERTAÇÃO SUBMETIDA AO CORPO DOCENTE DO INSTITUTO ALBERTO
LUIZ COIMBRA DE PÓS-GRADUAÇÃO E PESQUISA DE ENGENHARIA (COPPE)
DA UNIVERSIDADE FEDERAL DO RIO DE JANEIRO COMO PARTE DOS
REQUISITOS NECESSÁRIOS PARA A OBTENÇÃO DO GRAU DE MESTRE EM
CIÊNCIAS EM ENGENHARIA CIVIL.

Examinada por:



Prof. Paulo Couto, Dr. Eng.



Prof. José Luis Drummond Alves, D.Sc.



Dr.ª Giovanna da Fraga Carneiro, D.Sc.

RIO DE JANEIRO, RJ - BRASIL

SETEMBRO DE 2019

Dantas da Silva, Marianna

Study of the Representative Elementary Volume Of
Carbonate Rocks And Pore Network Simulation/ Marianna

Dantas da Silva – Rio de Janeiro: UFRJ/COPPE, 2019.

XVII, 84 p.: il.; 29,7 cm.

Orientador: Paulo Couto

Dissertação (mestrado) – UFRJ/ COPPE/ Programa de
Engenharia Civil, 2019.

Referências Bibliográficas: p. 80-84.

1. Microtomografia. 2. Pore Network Models. 3.
Representative Elementary Volume. I. Couto, Paulo. II.
Universidade Federal do Rio de Janeiro, COPPE, Programa
de Engenharia Civil. III. Título.

Para os meus pais, por toda a dedicação,

Linda and Dinalto.

AGRADECIMENTOS

Agraço primeiramente à minha grande família, fonte de inspiração e perseverança. Em especial agradeço a minha avó, Terezinha Dantas, que nos ensinou o poder e o valor da educação.

Agradeço ao meus pais, pelo empenho para que eu sempre tivesse a melhor educação, pelo apoio durante os anos longe de casa. Agradeço imensamente à minha mãe, Linda, pelo apoio incondicional em todos os momentos.

Agradeço ao meu irmão, Rafael, por nossa cumplicidade.

Agradeço às minhas segundas mães, Ana, Norma e Tetina pelo incentivo e suporte.

Agradeço ao meu orientador, Paulo Couto, pelo apoio, sugestões e a oportunidade do desenvolvimento desse trabalho.

Agradeço à Betty May, especialmente por sua generosidade, que tornou a conclusão deste trabalho possível. Você abriu portas.

Agradeço à equipe do LRAP pelo apoio nas dúvidas, dados, experimentos e conhecimento compartilhado. Agradeço também aos grupos do LIN/UFRJ e Ufflar pelos experimentos realizados, e ao Prof. Amir Raoof, da Utrecht University pela utilização do PoreFlow e as suas contribuições técnicas.

Agradeço à Schlumberger pela oportunidade de estágio e posteriormente trabalho durante o desenvolvimento desta dissertação. Agradeço também aos meus amigos de trabalho, Vanessa Simões, Patrick Machado, Giovanna Carneiro e Flavio Ferreira, pelo apoio, compreensão e inúmeras discussões.

Agradeço às minhas amigas de graduação, mestrado e vida, Adna, Jeniffer e Horrara, e aos novos amigos do mestrado Cleriston e Ana Paula, pelo companheirismo e por compartilhar os finais de semana de estudo.

À CAPES pelo suporte financeiro.

À Deus, por todos os pedidos de ajuda atendidos.

Resumo da Dissertação apresentada à COPPE/UFRJ como parte dos requisitos necessários para a obtenção do grau de Mestre em Ciências (M.Sc.)

ESTUDO DO VOLUME ELEMENTAR REPRESENTATIVO DE ROCHAS CARBONÁTICAS E SIMULAÇÃO DE REDE POROSA

Marianna Dantas da Silva

Setembro/2019

Orientador: Paulo Couto

Programa: Engenharia Civil

A caracterização de reservatórios carbonáticos é um desafio importante enfrentado pela indústria brasileira de O&G. Nesse contexto, os estudos e a simulação de modelos tridimensionais de rochas digitais estão sendo desenvolvidos como uma ferramenta para auxiliar na caracterização petrofísica de tais rochas. Essa tecnologia utiliza imagens de tomografia microcomputadorizada (micro-CT), um método não destrutivo que permite a investigação da estrutura interna de rochas em escala de poros. O objetivo deste estudo é utilizar modelos de rochas digitais 3D para entender o Volume Elementar Representativo (REV) dos carbonatos heterogêneos, rochas de coquina e calcário, simular Modelos de Rede de Poros (PNM) e, a partir análise estatística, reproduzir e simular PNMs sintéticos. Metodologia que pode ser usada em estudos posteriores, na transferência de escala dos modelos de espaço de poros das rochas. Além disso, o objetivo deste estudo é desenvolver modelos de rochas digitais 3D correlacionados à diferentes técnicas de caracterização do espaço poroso, como imagens de micro-CT e medidas de RMN T_2 . As amostras de rocha foram submetidas à três medições laboratoriais: análise de rotina de plugue, experimentos de RMN T_2 e aquisição de imagens de micro-CT em diferentes resoluções. Os resultados dos modelos digitais 3D incluem estimativas de porosidade e permeabilidade, simulação de PNMs, impacto das resoluções de imagem nos modelos, análise da distribuição do tamanho dos poros, número de coordenação, estudo de REV, e os PNMs sintéticos representativos. Além disso, os resultados de porosidade e permeabilidade obtidos através de simulações foram comparados com as medições laboratoriais.

Abstract of Dissertation presented to COPPE/UFRJ as a partial fulfillment of the requirements for the degree of Master of Science (M.Sc.)

STUDY OF THE REPRESENTATIVE ELEMENTARY VOLUME OF CARBONATE ROCKS AND PORE NETWORK SIMULATION

Marianna Dantas da Silva

September/2019

Advisor: Paulo Couto

Department: Civil Engineering

Carbonate reservoir characterization is an important challenge faced by the Brazilian O&G industry. In this context, the studies and simulation of three-dimensional digital rock models are being developed as a tool to aid in the petrophysical characterization of such rocks. This technology uses micro-computed tomography (micro-CT) images, which is a non-destructive method that allows the investigation of internal structure of rock at pore scale. The objective of this study is to use 3D digital rock models to understand the Representative Elementary Volume (REV) of heterogeneous carbonates, coquina and limestone rocks, simulate Pore Network Models (PNM) and from statistical analysis reproduce and simulate synthetic PNMs. Methodology that, may be used in further studies to upscale rocks' pore space models. Additionally, the aim of this study is to develop 3D digital rock models that are correlate to different pore space characterization techniques such as micro-CT images and NMR T_2 measurements. The rock samples were submitted to three laboratory measurements: routine core analysis, NMR T_2 experiments, and micro-CT scans at different resolutions. The results of the 3D digital models include porosity and permeability estimations, simulation of PNMs, impact of image resolutions on models, analysis of pore size distributions, coordination number, REV study and the representative synthetic PNMs. Moreover, results for porosity and permeability obtained through simulations were compared to the laboratory measurements.

INDEX

INDEX VIII

LIST OF FIGURES	XI
LIST OF TABLES	XV
NOMENCLATURE	XVI
1 INTRODUCTION	1
1.1 Context and Motivation	1
1.2 Objectives	1
1.2.1 Specific Objectives	2
1.3 Dissertation Workflow.....	2
2 LITERATURE REVIEW	4
2.1 Petrophysics.....	4
2.1.1 Porosity	5
2.1.2 Permeability	6
2.2 Digital Petrophysics.....	7
2.3 Micro Computed Tomography	8
2.4 Pore Network Model and Fluid Flow Simulation.....	9
2.4.1 Synthetic Pore Network Models	12
2.5 Nuclear Magnetic Resonance	15
2.6 Carbonates Heterogeneity and Upscaling.....	18
2.7 Representative Elementary Volume	19
3 METHODOLOGY	22
3.1 Samples.....	22
3.2 Data Acquisition	23
3.2.1 Routine Petrophysics Analysis	23
3.2.1.1 Porosity and grain density	23
3.2.1.2 Permeability.....	24
3.2.2 Micro-CT Images Acquisition	25
3.2.3 NMR Experiments	26
3.3 NMR Processing.....	26
3.3.1 NMR T ₂ Pore Size Curves	26
3.4 Micro-CT Images Processing	28
3.4.1 Pre-Processing	28

3.4.2	Region of Interest.....	28
3.4.3	Segmentation	29
3.4.4	Three-Dimensional Digital Rock Model	31
3.4.5	Porosity	31
3.4.6	Micro-CT Pore Network Modeling	31
3.4.6.1	Statistical Processing	34
3.4.7	Fluid Flow Simulation and Permeability	35
3.5	REV	35
3.6	Synthetic PNM generation.....	37
4	RESULTS AND DISCUSSION	38
4.1	Data Acquisition	38
4.1.1	Routine Petrophysics Analysis	38
4.1.2	Micro-CT Images Acquisition	38
4.1.3	NMR Acquisition and Processing.....	39
4.2	Micro-CT Images Processing	44
4.2.1	Pre-Processing	45
4.2.2	Segmentation and Porosity	46
4.2.3	Micro-CT Pore Network Models.....	48
4.2.4	Fluid Flow Simulation and Permeability Estimation.....	49
4.2.5	Impact of Micro-CT Resolution on Pore Network Distributions.....	51
4.3	REV Analysis	53
4.3.1	Porosity REV	53
4.3.2	Permeability REV	57
4.4	Pore Network Simulation.....	62
4.4.1	Micro-CT Pore Network Statistics.....	62
4.4.1.1	Coquina Sample 1_34A – 18 microns.....	62
4.4.1.2	Edwards Brown Sample EB_3 – 12 microns	64
4.4.2	Comparison of Micro-CT and Synthetic Pore Network Models	66
4.4.2.1	Coquina 1_34A – 18 μ m – Original Network Inputs	66
4.4.2.2	Coquina 1_34A – 18 μ m – PDF Distribution Inputs.....	70
4.4.2.3	Limestone EB_3 – 12 μ m – Original Network Inputs.....	72
4.4.2.4	Limestone EB_3 – 12 μ m – PDF Distribution Inputs	75
5	CONCLUSIONS	78
5.1	Further studies	79

6	BIBLIOGRAPHY	80
----------	---------------------------	-----------

LIST OF FIGURES

Figure 1: Workflow applied in this dissertation for development of 3D digital rocks, REV analysis and PNM simulation.....	3
Figure 2: X-ray apparatus scheme (Bultreys <i>et al.</i> , 2016).....	9
Figure 3: Representation of a section of pore space, its medial axis and throats identified by applying a medial axis algorithm. Reproduced from Bultreys <i>et al.</i> , 2016.....	10
Figure 4: Maximal ball algorithm classification of pore bodies in families A and B, which are represented by an ancestor (pore) and throats (connecting spheres). Reproduced from Bultreys <i>et al.</i> , 2016.....	10
Figure 5: Pore network model represented by simplified geometries, such as spheres and cylinders. Reproduced from de Vries <i>et al.</i> , 2017.....	11
Figure 6: Pore space representation considering grains as perfect spheres in yellow, pores with sphere shape in blue, and throats with sphere shape in red.	13
Figure 7: a) Thin-section Fontainebleau sandstone. The pore space is shown in white and the grain in black. Reproduced from Okabe and Blunt, 2005. b) Cropped area from yellow square in picture a. c) Drawing of the representation of the pore space with simplified geometries. The grains are represented in yellow and pore space in gray. Blue sphere represents a pore and in red the throats.	14
Figure 8: Segmented micro-CT image from Coquina. The pore space is shown white and the grain black. b) Cropped area from yellow square in picture a. c) Drawing of the representation of the pore space with simplified geometries. The grains are represented in yellow and pore space in gray. Blue sphere represents a pore and in red the throats. ...	14
Figure 9: T2 decay for different and singles pores and final result. Reproduced from Coates (1999).....	17
Figure 10: Inversion process of T2 echo train to T2 distribution vs porosity increment. Reproduced from Souza, 2012.	18
Figure 11: Example of non-overlapping subvolumes extracted from a borehole- to interwell-scale model.....	20
Figure 12: On the left the Edwards Brown samples: EB_1 (slab), EB_2 (1/4 of the slab EB_1), EB_3 (short plug) and EB_4 (long plug); and in the right the Coquina sample 1_34A.	23

Figure 13: CT Scanner SkyScan 1173 at LIN/UFRJ.....	25
Figure 14: a) ROI selection with Volume Edit tool; b) Cropped region.	29
Figure 15: a) Original image; b) Segmented space visualization using Interactive Threshold; c) Segmented image in pore space (black), rock matrix (white) and exterior region (blue).	30
Figure 16: Maximal balls representation of the throats connects two pores (N_1 and N_2)	33
Figure 17: Representation of the network conversion from the maximal-balls geometry to represent the throats from spheres to cylinder.....	34
Figure 18: Segments connecting the same pore-bodies that were excluded from the PNM.	34
Figure 19: Workflow to crop subsamples from the rock plug for REV study.	36
Figure 20: NMR T_2 curve for the sample 1_34A.	39
Figure 21: NMR T_2 curve for the sample EB_4, 1 st measurement.....	40
Figure 22: NMR T_2 curve for the sample EB_4, 2 nd measurement.	40
Figure 23: NMR T_2 pore size distribution curve for the sample 1_34A (blue line) and fraction of the curve that can be observed from the micro-CT image at resolution of 18.16 μm (dashed red line).	42
Figure 24: NMR T_2 pore size distribution curve for the sample EB-4 (1 st measurement) in the blue line and fraction of the curve that can be observed from the micro-CT image at resolution of 17.81 μm in the dashed red line.	43
Figure 25: NMR T_2 pore size distribution curve for the sample EB-4 (2 nd measurement) in the blue line and fraction of the curve that can be observed from the micro-CT image at resolution of 17.81 μm in the dashed red line.	43
Figure 26: Micro-CT image of: a) EB_3 (18 μm); and b) 1_34A (18 μm)	45
Figure 27: Comparison of raw image (a) and filtered by Non-Local Means (b) of sample EB_3.	46
Figure 28: Comparison of the threshold value and resultant porosity estimated from the micro-CT images.	47
Figure 29: a) 3D rock model and b) pore space segmented model of EB_3.....	48
Figure 30: Sample EB_3: a) 3D models of rock sample and connected pore space in blue; b) All pore space segmented; c) Connected pore space; and d) Pore space skeleton.....	49

Figure 31: Pore network final pressure gradient during the fluid simulation of a) 1_34A and b) EB_3.....	50
Figure 32:a) EB_1 sample; b) Division in 4 subsamples; c) Micro-CT image o EB_1 with 12.26 μm ; d) Top of subsample EB_2 from EB_1; e) Bottom of subsample EB_2; and f) Micro-CT image of subsample EB_2.....	51
Figure 33: Density plot of the PNM pore size distribution of the same area of sample EB_1 at resolutions of 7 and 12 μm	52
Figure 34: Density plot of EB_3 sample at resolutions of 12 and 18 μm	53
Figure 35: REV analysis for porosity of sample 1_34A.	54
Figure 36: REV analysis for porosity of sample EB_1.	56
Figure 37: VER analysis for porosity of sample EB_3.	57
Figure 38: REV analysis for permeability of sample 1_34A.	58
Figure 39: REV analysis for permeability of sample EB_1.	60
Figure 40: REV analysis for permeability of sample EB_3.	61
Figure 41: a) Pore size radius histogram and gaussian fit of sample 1_34A; b) Cumulative distribution of the fit.....	62
Figure 42: a) Pore throat radius histogram and gaussian fit of sample 1_34A; b) Cumulative distribution of the fit.	63
Figure 43: a) Throat length histogram and gaussian fit of sample 1_34A; b) Cumulative distribution of the fit.....	63
Figure 44: Coordination number histogram of sample 1_34A.....	64
Figure 45: a) Pore size radius histogram and gaussian fit of sample EB_3; b) Cumulative distribution of the fit.....	65
Figure 46: a) Pore throat radius histogram and gaussian fit of sample EB_3; b) Cumulative distribution of the fit.....	65
Figure 47: a) Throat length histogram and gaussian fit of sample EB_3; b) Cumulative distribution of the fit.....	66
Figure 48: Coordination number histogram of sample EB_3.	66
Figure 49: Sample 1_34A synthetic PNM a) Pore sizes; b) Inlet and outlet zones for fluid flow; and c) Final pressure gradient of fluid flow.....	69
Figure 50: Sample 1_34A micro-CT PNM a) Pore sizes; b) Inlet and outlet zones for fluid flow; and c) Final pressure gradient of fluid flow.....	69

Figure 51: Pore networks and connections of a) 1_34A synthetic network; and b) 1_34A micro-CT network. 70

Figure 52: Sample EB_3 synthetic PNM a) Pore sizes; b) Inlet and outlet zones for fluid flow; and c) Final pressure gradient of fluid flow. 73

Figure 53: Sample EB_3 micro-CT PNM a) Pore sizes; b) Inlet and outlet zones for fluid flow; and c) Final pressure gradient of fluid flow. 73

Figure 54: Sample EB_3 synthetic PNM with modified input zone a) Pore sizes; b) Inlet and outlet zones for fluid flow; and c) Final pressure gradient of fluid flow..... 75

LIST OF TABLES

Table 1: Rock samples studied, type o data acquisition and dimensions.....	22
Table 2: Samples acquisition and reconstruction time.....	25
Table 3: Rock samples surface relaxivity.....	27
Table 4: RCA for samples studied.....	38
Table 5: Samples micro-CT number of images and resolution.....	39
Table 6: Rock samples analyzed for surface relaxivity and maximum porosity evaluated for micro-CT resolutions.....	41
Table 7: Maximum porosity estimated for each micro-CT resolution based on NMR T_2 pore size distribution.....	44
Table 8: Thresholds evaluated for images segmentation.....	47
Table 9: Comparison of porosities expected at each resolution and result porosity value for threshold.....	48
Table 10: Permeability results comparison.....	49
Table 11: Subsamples Division volumes in mm^3	53
Table 12: Results for porosity REV analysis of sample 1_34A.....	55
Table 13: Results for porosity REV analysis of sample EB_1.....	56
Table 14: Results for porosity REV analysis of sample EB_3.....	57
Table 15: Results for permeability REV analysis of sample 1_34A.....	59
Table 16: Results for permeability REV analysis of sample EB_1.....	60
Table 17: Results for permeability REV analysis of sample EB_2.....	61
Table 18: Parameters statistics for micro-CT and synthetic (original network inputs) PNM models of sample EB_3.....	68
Table 19: Parameters statistics for micro-CT and synthetic (statistical distributions) PNM models of sample 1_34A.....	71
Table 20: Parameters statistics for micro-CT and synthetic (original network inputs) PNM models of sample EB_3.....	74
Table 21: Parameters statistics for micro-CT and synthetic (with modified input layer) PNM models of sample EB_3.....	75
Table 22: Parameters statistics for micro-CT and synthetic (statistical distributions) PNM models of sample EB_3.....	77

NOMENCLATURE

Symbols

A	-	Area
C_v	-	Coefficient of variability
I	-	X-ray intensity
L	-	Length
K	-	Permeability
mm	-	Millimeter
M	-	Magnetization
mg	-	Milligrams
N or n	-	Number
R or r	-	radius
<i>P</i> or p	-	Pressure
ppk	-	Parts per thousand
psi	-	Libra-força por polegada quadrada
<i>Q</i>	-	Fluid flow
q	-	Volume flow rate
s	-	seconds
t	-	time
T_2	-	Relaxation time
S	-	Surface
μm	-	micrometer
μs	-	microsecond
V	-	Volume
\bar{x}	-	Mean

Greek Letters

ρ_2	-	Surface relaxivity
σ	-	Standard deviation
μ	-	Viscosity
μ	-	Linear attenuation coefficient
Φ	-	Porosity

Abbreviations

ANP	-	Agência Nacional do Petróleo, Gás Natural e Biocombustíveis
PNM	-	Pore Network Model
Micro-CT	-	Micro Computed Tomography
NMR	-	Nuclear Magnetic Resonance
REV	-	Representative Oil in Place

1 INTRODUCTION

1.1 CONTEXT AND MOTIVATION

In Brazil, 56% of the actual proven reserves are originated from the Pre-salt cluster reservoirs (Kury, 2019). These reservoirs are mostly formed by carbonate rocks, which are well known by the challenges addressed by their properties heterogeneity.

Reservoir characterization is usually performed by studies on core plug samples and well logs. Inevitably, these two can cover an area of only a few meters from the wellbore, and indeed are applied to understand the behavior of a kilometer scale volume, in the case of the giant fields in the Brazilian coast. Furthermore, a challenge that is addressed by some authors (Ferreira *et al.*, 2018; Huang *et al.* 1997) is the difficulty faced to perform special core analyses measurements for motives that encompass time long lasting experiments or the difficult to reproduce reservoir conditions.

Digital petrophysics, treated in this dissertation as the study of three-dimensional digital models from micro-computed tomography (micro-CT), may aid in some aspects of the issues faced by laboratory measurements, whether it be by the facility of reproducibility of experiments, time or the non-destructive characteristic of this technique. However, this methodology faces its own challenge regarding data management. Large samples cannot be imaged at high resolutions due to impracticable data size, while smaller samples may be imaged at enough good resolution but may not be representative of the rock properties. The latter is especially true for Brazilian carbonates reservoirs that present a high heterogeneity.

1.2 OBJECTIVES

Considering the challenges mentioned in the previous section, the main objective of this study is to understand the Representative Elementary Volume (REV) of the samples studied, simulate Pore Network Models (PNM) and from their statistics reproduce and simulate synthetic PNM. Methodology that, may be used in further studies to upscale rock pore space models. Additionally, the aim of this study is to develop digital

rock models that can correlate different pore space characterization techniques such as micro-CT images and NMR measurements.

1.2.1 Specific Objectives

Within the spectrum of this study, the specific objectives are:

- a) Acquisition of micro-CT images with different resolutions and samples sizes.
- b) Micro-CT images processing towards the achievement of petrophysical properties as porosity and permeability.
- c) Generate PNMs based on micro-CT images and following PNM statistics.
- d) Acquisition of NMR T_2 experiments of samples, and inversion of T_2 to pore-size distribution using surface relaxivity.
- e) REV study for porosity and permeability of samples.
- f) Results analysis and correlation of petrophysical properties among laboratory measurements, micro-CT based models and synthetic PNMs.

1.3 DISSERTATION WORKFLOW

This dissertation is organized in Introduction, Literature Review, Methodology, Results and Discussion and Conclusions.

Chapter 1 presents an introduction to the theme proposed, focusing on the definition of the problem, general and specific objectives, and the dissertation organization.

Chapter 2 presents the literature review, which expose sprevious studies published in petrophysics, micro computed tomography as a source for three-dimensional digital rock models, nuclear magnetic resonance background and T_2 measurements, carbonate reservoirs heterogeneity and challenges for their properties characterization, simulation of PNMs and fluid flow and REV studies.

Chapter 3 presents the materials used in the developments of this study as well as the methodologies applied in laboratory measurements, micro-CT images processing, NMR T_2 inversion, correlations of pore-size distributions, REV study, simulation of micro-CT, statistical analysis and synthetic PNM generation.

Chapter 4 presents the results regarding the methodologies applied and the discussion around the properties estimated, the problems encountered and correlation between methods.

Chapter 5 presents the conclusion of this study according to the initial specific objectives set and suggestions for further studies.

The workflow proposed in this dissertation follow the organogram below and it is divided into four main sections: 1) Laboratory acquisition of petrophysical data, micro-CT images and NMR T₂ curves; 2) development of 3D digital rock models; 3) REV analysis for the 3D digital rock models; and 4) synthetic PNM simulation.

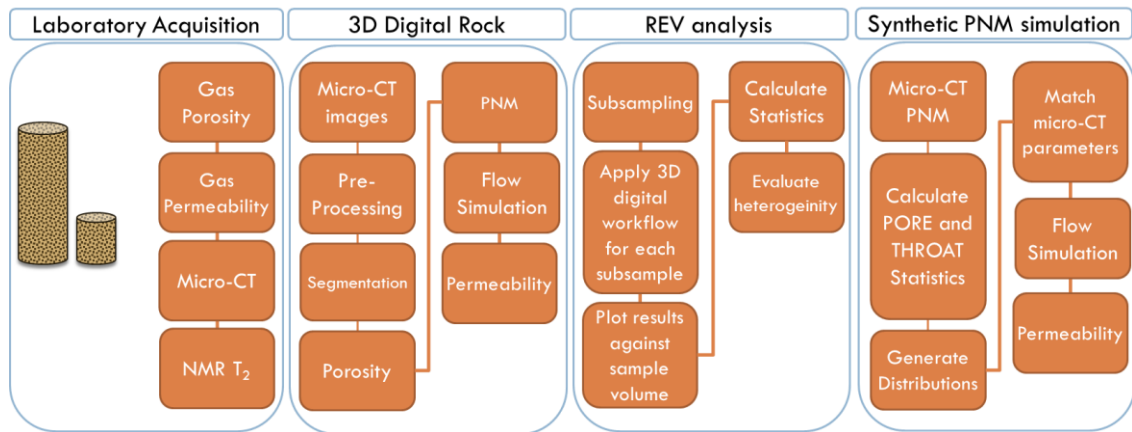


Figure 1: Workflow applied in this dissertation for development of 3D digital rocks, REV analysis and PNM simulation.

2 LITERATURE REVIEW

2.1 PETROPHYSICS

Petrophysics is the study of rock and fluids properties and their interaction (Tiab and Donaldson, 2004). Particularly, its purpose is identifying how minerals constitute rocks and the amount and how fluids saturate them. In Petroleum Engineering, the rocks that comprise a reservoir and are subject for study are mostly sedimentary rocks, and in singular cases, igneous or metamorphic rocks that may compose a Petroleum System. In fact, the valuable information retrieved from them is concerned to their function as a source of hydrocarbons (Kennedy, 2015).

In general, petrophysics uses inverse problems to determine the following three reservoir properties:

- Porosity: a measure of the void space;
- Saturation: a measure of type and quantity of fluid within the void space;
- and Permeability: the ability of a rock to allow fluid flow (Kennedy, 2015).

Reservoir rocks may present low to high values of porosity, according to Lucia (2007) they range from 1 to 35% in carbonates; and the network in which this pore space is connected is an important feature for permeability. These two properties together will influence the quantification of storage and transmissibility of the hydrocarbon fluids present in the pores (Tiab and Donaldson, 2004). This work focuses on the study of these two properties by the correlation of laboratory measurements and digital rock models.

The firsts studies on petrophysics date from the 1920's and were developed by Kozeni and Conrad and Marcel Schlumberger. Kozeni solved the Navier-Stokes equation for fluid flow by considering a porous medium in order to obtain a relationship among porosity, permeability and surface area. Later, the Schlumberger brothers developed the first well logging technology, the Resistivity Log, which presented primary indications of lithology and fluid saturation. In 1942, Archie published studies that made it possible to quantify porosity from well logging resistivity data. Years later he decided to name the studies specialized on rock and fluid properties Petrophysics. Therefore, the correlation of laboratory experimental data, well logging, production teste data, outcrops rocks and

petroleum systems are the pillars of Petrophysics (Kennedy, 2015, Tiab and Donaldson, 2004).

Petrophysical properties of sedimentary rocks are controlled by the depositional environment they were formed in, and also by the changes that occurred in the sediments after their deposition (diagenesis). These factors will influence the rock's mineral composition, grain size, orientation or packing, amount of cementation, and compaction. The understanding of the sedimentary processes can be done by observing how sediments are formed today, as we can correlate them to the formation processes of actual sedimentary rocks that compose a reservoir (Tiab and Donaldson, 2004 and Bjorlykke, 2010).

2.1.1 Porosity

Porosity is a measure of the void space within a volume of rock and defines the potential storage for hydrocarbons. According to Tiab and Donaldson (2004), the grains and particles that form a rock present irregular shapes, therefore their packing arrangement is never perfect, and the void space is generated. Generally, the porosity can be classified in primary and secondary and also in terms of absolute and effective porosity.

During sedimentation and lithification, some pore spaces became isolated due to diagenetic and catagenetic processes, considering that, the effective porosity corresponds to the pore space that is connected and is available for fluid flow, while the absolute porosity represents the total pore space (Lucia, 2007 and Tiab and Donaldson 2004).

Moreover, according to the origin of the pore, porosity can be classified as primary (the pore was formed in de the deposition process) or secondary (the pore was created as a result of subsequent process, as diagenesis for example).

The types of primary porosity as described in Tiab and Donaldson (2004) are:

- Intercrystalline voids: voids between individual crystals, or cleavage plane of crystals, or in crystal lattices;
- Intergranular or interparticle voids: voids between grains

- Bedding plane voids: voids that are concentrated in parallel to bedding planes; and
- Miscellaneous sedimentary voids: voids resultants from created by living organisms at the time of deposition or vuggy or cavernous voids formed at the deposition.

And, the secondary porosity can be described as:

- Solution porosity: channels formed or enlarged during the circulation of fluids;
- Dolomitization: the process in which limestone, when in contact with water is transformed into dolomite;
- Fracture porosity: fractures originated by tension forces; and
- Miscellaneous secondary voids: other type of voids resultant from any bed or material movement.

Porosity may also be classified in terms of its pore size, as microporosity, mesoporosity and macroporosity (Westphal, 2005; Choquette and Pray, 1970). Quantitatively, porosity is denoted by ratio between the pore volume (V_p) and the bulk volume (V_b) (Eq. 2.1).

$$\Phi = \frac{V_b - V_{gr}}{V_b} = \frac{V_p}{V_b} \quad (2.1)$$

Where Φ represents porosity and V_{gr} is the volume of grains.

2.1.2 Permeability

According to Lucia (2007) permeability is a property that relates the rate that hydrocarbons can be produced from a reservoir, it is a measure of the ability to allow fluid flow through the connected pore space without considering any movement of the matter. After the studies developed by the engineer Henry Darcy, the permeability can be described by equation 2.2. Considering a single phase in the fluid, it is classified as absolute permeability. In the presence of other fluids such as oil or gas, it is classified as

effective permeability. Its values may range significantly from less than 0.01 millidarcy (mD) to well over 1 Darcy (Tiab and Donalson.2004).

$$k = \frac{\mu Q L}{A \Delta P} \quad (2.2)$$

Where k is permeability, μ is fluid viscosity, Q is rate of flow, ΔP is the differential pressure between the inlet and outlet of the sample teste, and L and A refers to the geometrical characteristics of sample length and area, respectively.

At the pore scale perspective, pore space geometry and topology are important features that will influence flow and transport in porous media, and therefore impact macroscopic variables such as permeability (Yang *et al.*, 2016). Geometry parameters are related to the pore space properties such as pore/throat sizes and shapes distribution. On the other hand, topological parameters can be defined as discretization of pore space in pore or throats and number of throats connecting each pore. These properties will further be characterized in section 2.4.

2.2 DIGITAL PETROPHYSICS

The digital petrophysics is the study to better understand of the rock pore space and its petrophysical properties by using three dimensional digital models. This technology uses image data to retrieve 2D and 3D properties of rock samples that can cover space resolution from nanometers to a few meters (Bultreys, 2016). The 2D analysis is commonly performed by traditional microscopy on thin sections and can provide an accessible study of porosity, grain shape, type of porosity and brief estimations of permeability (Lucia, 2007).

The use of micro-CT for 2D, and mostly 3D digital rock analysis had been established in the last decade. According to Blunt (2013) the first micro-CT scans of rocks were acquired by Flannery and co-workers at Exxon Research Center, followed by Dunsmuir, who extended the work by characterizing pore space and fluid flow in sandstones. Micro-CT images allows the investigation of the internal structure of a material, and, for petrophysical studies, rock samples can be analyzed by their surface

and internal features, such as beddings, sedimentary structures, diagenetic characteristics, cementation, grains morphology and density (Cnudde and Boone, 2013).

The 3D rock models are generated by stacking a assemble of images and segmenting them into different phases, that is, clustering different ranges of gray tone that represent a material into discrete phases. To process and analyze these images there are a variety of software packages available in the industry, such as Avizo, VGS Studio Max, MAVI, BLOB3D, Pore3D and ImageJ (fiji) (Cnudde and Boone 2013). Besides that, the application of program languages such as Python or MATLAB are being implemented for this purpose. The range of data retrievable from those analyses is wide, and include porosity, permeability, surface to volume ratio, mineralogy, grain and pore morphology, pore network models and properties spatial variation (Raof and Hassanizadeh, 2013; Bultreys *et al.*, 2016; Xiong *et al.* 2016).

2.3 MICRO COMPUTED TOMOGRAPHY

Micro-CT Scanners are a non-destructive 3D imaging technology used for investigation of the internal structure of materials. In the Petroleum Industry they have been applied mainly for the study of fluid flow and rock characterization (Hu *et al.*, 2014, Blunt *et al.*, 2013). This imaging technique allows the investigation of structure in the scale range of micrometers up to a few millimeters. This technique uses the capability of radiation to penetrate materials in varying degrees. The penetration happens due to two mechanisms, the absorption of the photon by photoelectric effects or Compton scattering (Andreeta, 2017). According to Andreeta (2017), the photoelectric effect is the absorption of energy from a high energetic photon to an electron in the material exposed to radiation, while the Compton scattering represents the loss of energy of the photon due to its interaction with a weakly bounded electron.

The x-ray attenuation is expressed by Lambert-Beer Law (Eq. 2.3):

$$I = I_0 e^{-\int \mu(s) ds} \quad (2.3)$$

Where I is the transmitted X-ray intensity, I_0 the incident intensity and μ the linear attenuation coefficient of the material. The X-ray attenuation is dependent on the atomic number and density of the material (Cnudde and Boone, 2013, Bultreys *et al.*, 2016), thus

if the sample's material is heterogeneous, the attenuation value will vary along the sample, which will enable the internal mapping of the sample.

A typical lab-based micro-CT setup consists of a standard conical X-ray beam source and a detector, with the sample being rotated in between them (Figure 2). The resultant resolution of a micro-CT image is function of the distance the object is placed from the conical beam, but it is limited by the focal spot size of the assembly.

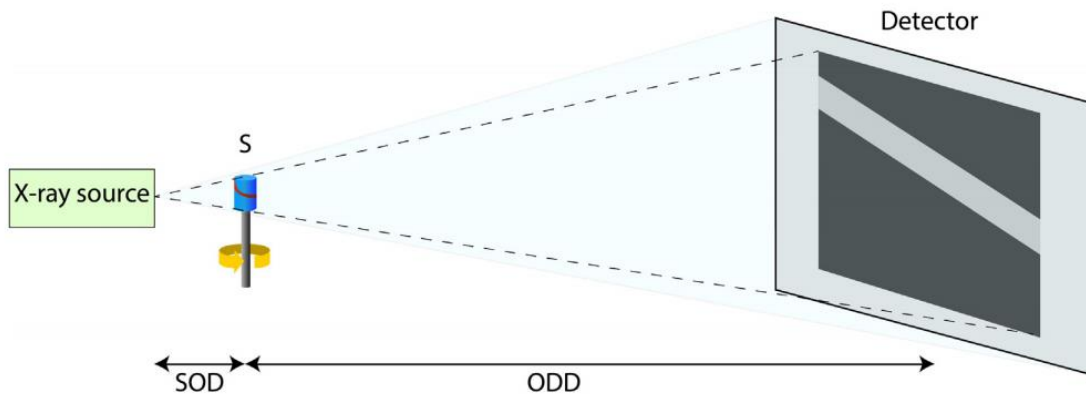


Figure 2: X-ray apparatus scheme (Bultreys *et. al.*, 2016).

According to Andreetta (2017), tomograms of the radiation projection over the sample are captured while they are rotating. Finally, processing algorithms are capable to invert the sequence of tomograms into images that represent slices of the internal structure of the sample along a given axis. The micro-CT images vary in gray-scale, where denser materials are represented by lighter tone, and low density materials such as air, is represented by black.

2.4 PORE NETWORK MODEL AND FLUID FLOW SIMULATION

One of the methods applied to simulate multi-phase flow in porous media at pore-scale and thus, to estimate petrophysical properties, are Pore Network Models (PNM) (Bultreys *et al.*, 2016). According to Blunt (2001), PNMs are a simplified representation of the complexity of the pore space with idealized geometries such as spheres. These models have been proved success in representing the multiphase behavior in a pore scale at a low computational cost (Blunt, 2001; Young *et al.*, 2016).

The pore space is continuous, and thus it can be discretized into elements. Pores can be identified as the larger open spaces, while pore-throats are characterized as constrictions to the flow. According to Bultreys *et al.* (2016), there are two classes of methods to discretize the pore space: topology-central methods and morphology central methods. The first, applies a medial axis algorithm, which is an approach to represent the pore space by a centralized skeleton that can be used to detect individual pores and throats (Figure 3). The latter, morphology-central methods, generally applies search vectors to first identify constrictions, and then characterize the pore. One of the morphology-methods applies a maximal-balls algorithm (Figure 4). This method runs a search vector and tries to fit the largest inscribed sphere centered on each image voxels defined as pore-space. Afterwards, the spheres are classified into families, where the largest balls are classified as family ancestors (pores) and the smallest, or narrow passages, to belonging to that family (throats) (al-Kharusi and Blunt, 2007).

The PNMs generated can capture important features that impact the fluid flow in porous media such as constrictions, pore-size distributions and number of pore connections to throats (coordination number) (Young *et al.*, 2016). To get estimates of permeability with those simplified geometry networks, one can simulate single-phase fluid flow in the network and apply Darcy’s equation to the volume.

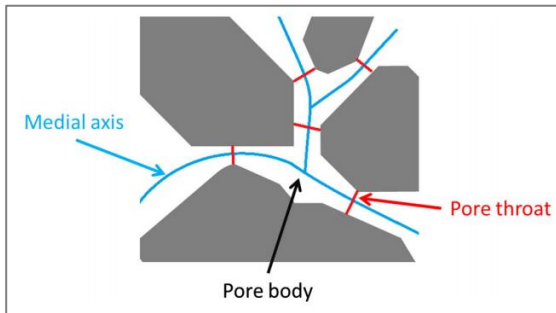


Figure 3: Representation of a section of pore space, its medial axis and throats identified by applying a medial axis algorithm. Reproduced from Bultreys *et al.*, 2016.

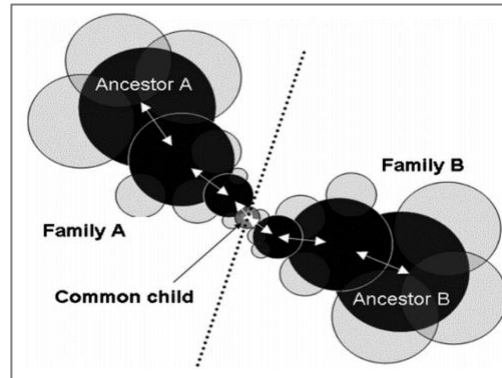


Figure 4: Maximal ball algorithm classification of pore bodies in families A and B, which are represented by an ancestor (pore) and throats (connecting spheres). Reproduced from Bultreys *et al.*, 2016.

PoreFlow (Raof *et al.*, 2013; Raof *et al.*, 2009; de Vries *et al.*, 2017) is pore-scale simulator with capabilities that includes pore network generation, drainage simulation, calculation of pressure and velocity distribution and modeling of flow and (reactive) transport in pore-scale. We apply this software package for PNM modeling and fluid flow simulation for permeability determination. In this application, the pore network model considers the porous medium as a system of pore elements composed of pore-bodies, which are denoted by spheres, and pore-throats, denoted as cylinders (Figure 5).

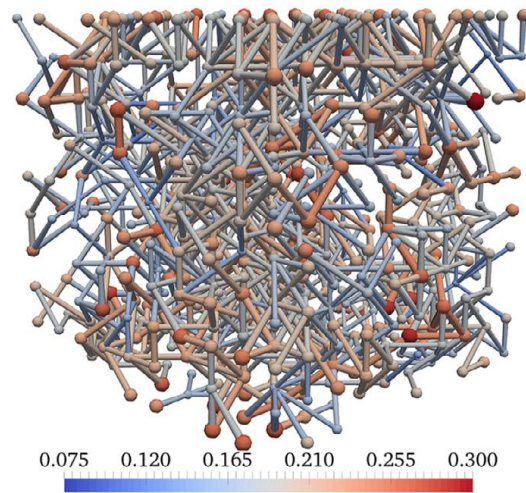


Figure 5: Pore network model represented by simplified geometries, such as spheres and cylinders. Reproduced from de Vries *et al.*, 2017.

The flow simulation in PoreFlow is performed by establishing a pressure difference across the network in one direction to meet a boundary condition of constant flow rate. According to Raof *et al.* (2009) and de Vries *et al.* (2017), the simulation considers that assuming a laminar flow for an incompressible fluid, the flow in a given pore throat ij can be defined by the Hagen-Poiseuille equation:

$$q_{ij} = g_{ij} (p_j - p_i) \quad (2.4)$$

where $q_{ij,tot}$ is the volumetric flow rate through a given pore throat ij , between the pore-bodies i and j , p_i and p_j are their respective pressures and g_{ij} is the conductance of

the throat, that can be represented as the Equation 2.5, if its geometry is considered as a cylinder:

$$g_{ij} = \frac{\pi R_{ij}^4}{8\mu l_j} \quad (2.5)$$

where μ represents the fluid viscosity, l represents the cylinder length, and R_{ij} the cylinder radius.

Assuming the condition of incompressible flow, where the sum of fluid into and out of a pore-body must be zero and given the z_i as the pore coordination number of pore i , the continuity equation may be considered as:

$$\sum_{j=1}^{z_i} q_{ij} = 0; \quad j = 1, 2, 3, \dots, z_i \quad (2.6)$$

Therefore, according to de Vries *et al.* (2017) the average fluid velocity can be defined as:

$$v = \frac{Q_{tot} L}{V_f} \quad (2.7)$$

where Q_{tot} is the total discharge of the pore network, L is the total length of the pore network, and V_f the total volume of fluid in the pore network. Therefore, the permeability of the pore network can be expressed as Darcy's equation below:

$$k = \frac{\mu Q_{tot} L}{A \Delta P} \quad (2.8)$$

where A is the cross-section area of the pore network and ΔP is the differential pressure between the pore network inlet and outlet.

2.4.1 Synthetic Pore Network Models

The study of pore networks models has been applied to understand the structure and the properties of porous media, and consequently, phenomena such as the capillary

effects that may affect the fluid flow in the pore space (Matadamas *et. al.*, 2014). The need for up-scaling of rock properties and the limitation of sample volume from micro-CT images at high resolution leads to the need for construction of statistically representative networks (Xiong *et al.*, 2016).

One of the challenges encountered in modeling synthetic PNMs is to represent the randomness found in rock pore space, represented by the topology and the heterogeneity of geometries. Most theoretical models of pore spaces apply perfect shapes to model rock grains and packing. In the Figure 6, a common representation of the definitions of pore space is represented. In this theoretical configuration, pores are regions of larger volume, and throats can be easily identified as the constrictions between the pores. In Figure 6, the rock grains are represented by the yellow spheres, the pore space is represented by the gray area, while the blue spheres represent a pore model, that is defined as the maximum spheres that can be inscribed into the pore space, and the red spheres represent the radius of the pore-throats.

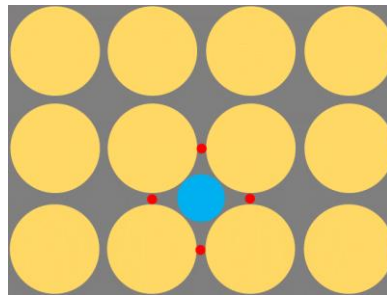


Figure 6: Pore space representation considering grains as perfect spheres in yellow, pores with sphere shape in blue, and throats with sphere shape in red.

The patterns described by the illustration are a large simplification of what happens in rocks real pore space. When analyzing a homogenous rock such as Fontainebleau Sandstone, similar patterns can be identified. In Figure 7, the packing, grain size and shape are overall keeping a homogeneous behavior, and this enables its patterns characterization. In comparison, in Figure 8, applying the same concepts for characterization, where grains may be represented by simplified geometries, identifying and quantifying a pore space or grain pattern may not be an easy task. The grains that compose the rock matrix present a large variety of geometry, packing aspects, cementing and diagenetic processes that altered the pore space configuration.



Figure 7: a) Thin-section Fontainebleau sandstone. The pore space is shown in white and the grain in black. Reproduced from Okabe and Blunt, 2005. b) Cropped area from yellow square in picture a. c) Drawing of the representation of the pore space with simplified geometries. The grains are represented in yellow and pore space in gray. Blue sphere represents a pore and in red the throats.

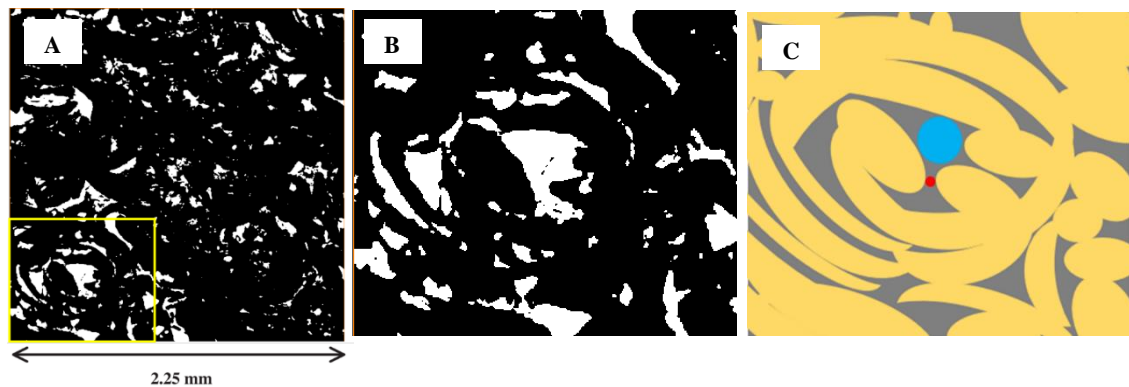


Figure 8: Segmented micro-CT image from Coquina. The pore space is shown white and the grain black. b) Cropped area from yellow square in picture a. c) Drawing of the representation of the pore space with simplified geometries. The grains are represented in yellow and pore space in gray. Blue sphere represents a pore and in red the throats.

When modeling pore networks, and if pores are represented by spheres, the radius of the pore is defined as the maximum inscribed spheres (represented by blue spheres in the previous images). Also, the throats radius may be defined as the maximum sphere radius inscribed into the throat regions, or either being a function of a set of spheres radius connecting the pores (represented by red spheres in the previous images). This type of modelling may be able to capture the aspects affecting fluid flow, but as the complexity of geometries and randomness of the pore space increases in the case of complex carbonate rocks is it still able to represent it?

Raouf and Hassanizadeh (2009) have developed a methodology to generate synthetic lattice-based network models that can model up to 26 pore connections in 13 different directions. This kind of modeling takes into account the topological randomness of porous media and reflects the multi-directionality of fluid flow in porous media. The method presents two elements: the pore bodies, located at the center of the lattice points, and the pore throats, connecting the pore bodies. To generate a wide distribution of coordination number, their method applies a bond elimination process. We apply this method for synthetic pore network models.

2.5 NUCLEAR MAGNETIC RESONANCE

Nuclear Magnetic Resonance (NMR) logging tools are widely used in formation evaluation to acquire estimates of permeability, porosity and pore size distribution, and they have an important application in circumstances in which classical logging techniques show insufficient sensitivity. NMR physical principles rely on the Hydrogen Nuclei Relaxometry, that is the response of a nuclei to a magnetic field. According to Kenyon (1997), hydrogen nuclei have a magnetic moment and spin, that, when exposed to an induced external magnetic field (B_0), get its spins gradually aligned towards the field B_0 . To study the relaxation behavior of the spin one applies radio-frequency pulses to generate a secondary magnetic field (B_1) which cause a perturbation in the thermal equilibrium between the spin orientation and the main magnetic field (B_0). The time in which the spin returns to its thermal equilibrium after the radio-frequency pulses are applied is the so called relaxation time.

In laboratory measurements, a sequence of Carr-Purcell-Meiboom-Gill (CPMG) radio-frequency pulses are emitted, with a magnetic field in different and rotating angles (Souza, 2016). This increases the signal available and reduces the effects of gradient magnetic field.

Hydrogen nuclei are mainly present in the fluid molecules confined inside the rock pores, and based on this fact, rock and fluids properties can be driven from such signal emitted by the magnetic field during the relaxation time. Kenyon (1997) attested that those relaxation times can be measured from both longitudinal and transverse proton

magnetization, which are two simultaneous and independent mechanisms (Souza, 2012) The curve entitled T_1 is the relaxation time correspondent to the longitudinal, that is, in the same direction as the external field applied to it. On the other hand, T_2 resembles the transversal relaxation time to the related field. T_2 relaxation curves were used in this study.

According to Coates (1999), when a wetting fluid fills a porous medium like a rock, T_2 decreases and the relaxation mechanisms are different from the measurements in only a solid or a fluid. In this case, the mechanism that rules T_2 are: bulk fluid, surface relaxation and diffusion. The equation that defines these three processes is:

$$\frac{1}{T_2} = \frac{1}{T_{2bulk}} + \frac{1}{T_{2surface}} + \frac{1}{T_{2diffusion}} \quad (2.9)$$

The bulk relaxation (T_{2bulk}) is the individual relaxation of the fluid, and it is related by its physical properties such as viscosity and molecular composition. The diffusion relaxation ($T_{2diffusion}$) occurs when fluids such as gas, light oil or water show a gradient magnetic field, as result the final T_2 is shortened. And finally, the surface relaxation ($T_{2surface}$), which is the response to the pore wall contact with the fluid saturating it (Kenyon, 1997). This effect provides sensitivity of NMR to pore size and brings the possibility to correlate rock parameters to it. The surface relaxation (Eq. 2.10) is controlled by surface relaxivity, which varies with the rock mineralogy.

$$\frac{1}{T_{2surface}} = \rho_2 \left(\frac{S}{V} \right) \quad (2.10)$$

In equation 2.10, S/V is a measurement of ratio of pore surface to volume. Thus, the lowest the surface by the volume ratio, the longest T_2 and larger the pore is. For lab-based rock NMR experiments, usually saturated with brine, the final T_2 is dominated by $T_{2surface}$, thus, the effect of the other components may be neglected. (Coates *et al.*, 1999, Westphal *et al.*, 2015, Souza *et al.* 2016).

Each rock will have a distribution of pore sizes, and each pore will have a singular S/V ratio, therefore, each of them will emit a single exponential decay T_2 . The sum of the exponential decay times of all pores is expressed by Equation 2.11:

$$M(t) = \sum M_i(0)e^{-t/T_{2i}} \quad (2.11)$$

Where $M(t)$ is the measured magnetization in function of time (t), $M_i(0)$ is the initial magnetization of the i th component and T_{2i} the decay constant of the i th component of relaxation.

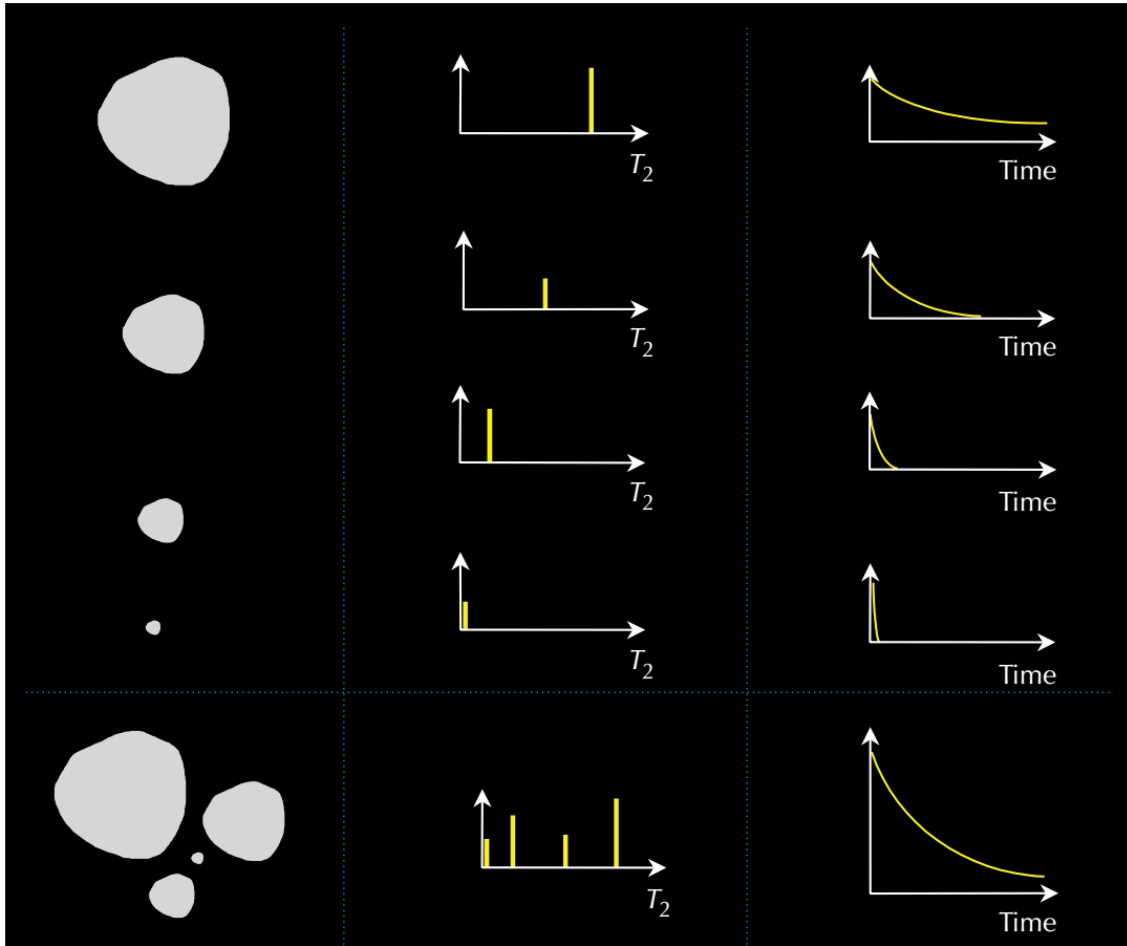


Figure 9: T2 decay for different and singles pores and final result. Reproduced from Coates (1999).

In Figure 9 the first column represents the pore size, the second column represents the T_2 value to the respective pore, and third column the T_2 exponential decay time. As T_2 equation 2.10 stated, considering pores of similar format, but varied sizes, the T_2 value will be higher for larger pores (low SV ratio) and the decay time will be larger - third column of Figure 9. The sum of all pores exponential decay, defined in equation 4, will result in the multiple T_2 values and a multi-exponential decay (last row of Figure 9).

To generate T_2 distribution, which will represent the pore T_2 peaks, the T_2 Echo train goes into a mathematical inversion using multi-exponential model, and the echoes are discretized in n different relaxation times with correspondent porosity increment components (Coates *et al.*, 1999). The following figure represents the multi-exponential echo train of T_2 and corresponding inversion of T_2 distribution as a function of the porosity increment.

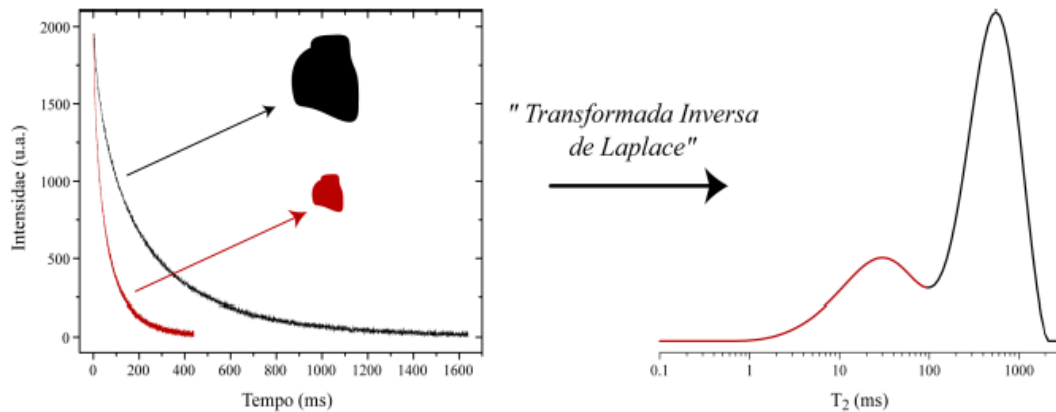


Figure 10: Inversion process of T_2 echo train to T_2 distribution vs porosity increment. Reproduced from Souza, 2012.

The interpretation of the T_2 distribution (Figure 10), in terms of pore-size, can be performed by the equation 2.10. Assuming the pore as spheres and knowing the rock surface relaxivity, T_2 can be converted to length, and analyzed as pore size (Souza *et al.*, 2016). According to Hoerlle *et al.* (2016) and Hoerlle *et al.* (2018), the pore-size distribution encountered in NMR T_2 can be correlated to the pore-size observed in the micro-CT images. Assuming the minimum diameter that a pore is identified in an image is represented by one single pixel, the micro-CT image is able to estimate pores with diameter above this resolution. Therefore, the micro-CT may be able to characterize up to the total porosity from the NMR pore-size distribution above that diameter

2.6 CARBONATES HETEROGENEITY AND UPSCALING

Carbonates reservoirs hold more than 60% of the oil and 40% of the gas volumes present in the world (Schlumberger, 2018). This type of reservoir is well known by its heterogeneous properties and the challenges addressed to its characterization. By definition, heterogeneity is the variation of reservoir properties as a function of space.

The heterogeneity is an intrinsic rock characteristic resultant of the sedimentary processes where the rock is originated since deposition and subsequent events. It is a scale-dependent property, that can vary in both microscopic and macro scale, as in vertical or horizontal directions (anisotropy) in a reservoir (Zhang, 2015; Hurley *et al.*, 2015; and Ahmed, 2006).

In carbonates, porosity heterogeneity can be represented by the different pore systems composing the pore space. The pore systems can be formed by the time of the deposition or created by diagenetic processes like dissolution or dolomitization. Intense dissolution may result for example, in the formation of highly permeable vugs or caverns. These processes can cause significant variation in the distribution of porosity and permeability of reservoirs. (Ferreira *et al.*, 2015; Tiab and Donaldson, 2004)

In this respect, permeability characterization poses a complex problem because its values can range by more than an order of magnitude in two neighbor regions and vary in a log-normal distribution. (Ahmed, 2006)

In Digital Petrophysics, advanced laboratory X-ray tomography equipment can retrieve a resolution of a few microns out of a rock volume of around 5 cm³ (Khalili *et al.*, 2012). Although this resolution may be good to resolve the pore scale, it may not represent the pore geometry heterogeneity. Upscaling properties measured in such a small scale make it challenging but very necessary when characterizing a reservoir. Different scales of upscaling involve different methodologies. They may be developed on properties from nanopore, to micro/meso or macropore network models, until lab plugs, whole cores, well logging and reservoir scale properties. Geostatistical methods are commonly used in the petroleum industry to quantitatively describe the heterogeneity (Zhang *et al.*, 2015; Ahmed, 2006). The motivation of this study is to contribute on studies for the upscaling of pore network models using data from rock core plugs.

2.7 REPRESENTATIVE ELEMENTARY VOLUME

REV, representative elementary volume, is a methodology developed to help to overcome the challenges addressed by heterogeneity and upscaling. According to Vik *et*

al. (2013), Corbett *et al.* (1999), Corbett *et al.* (2009) and Bear (1988), REV is defined as the minimum volume of certain property that is large enough to capture a representative amount of heterogeneity, or the minimum volume that is insensitive to small changes in volume or sample location. Note that REV may vary for different properties of the same rock sample, usually porosity REV is found in a smaller volume than permeability REV, due to the latter macroscopic variability. A specific objective of this study is to apply a REV analysis for porosity and permeability of carbonate rock samples.

According to Hurley *et al.* (2012), to determine a REV for such a rock property, a sample or a large volume model can be subsampled in a variety of scales, and the property be calculated as a function of volume. Nonetheless, an acceptance criterion of the property variation should be established so the subsample volume can be considered as REV. Additionally, the subvolumes extracted from a sample should be independent and non-overlapping volumes as showed in Figure 11.

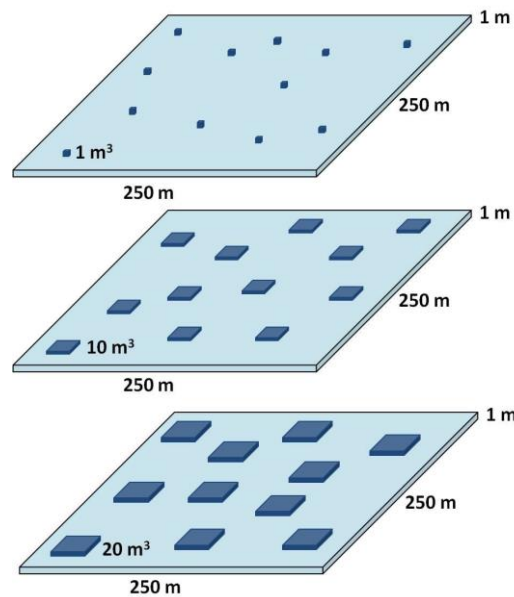


Figure 11: Example of non-overlapping subvolumes extracted from a borehole- to interwell-scale model.

A common methodology applied for a REV study defined in Hurley *et al.* (2012) consists of:

1. Measure a property in the entire sample volume
2. Subsample non-overlapping volumes inside the sample at different scale

3. Measure the property for each subsample
4. Analyze the given property as a function of sample volume
5. Determine an acceptance criterion for the property value variation
6. If the subsample attends the criteria it can be admitted as REV for the property

According to Vik *et al.* (2013), if the scale of a certain measurement, such as porosity, does not meet the minimum REV it may present a large variation of the property value. Studies to populate petrophysical properties in reservoir model apply average from measurements, therefore, if the measurements do not meet REV for samples sizes, and also present insufficient sample quantity (Corbett *et al.*, 1999), they may result in an incorrect representation of the reservoir real properties.

REV may show a complexity in carbonates, Khalili *et al.* (2013) performed a REV analysis for a heterogeneous carbonate and observed different REV's depending on the complexity of texture and the specific location of the subsample analyzed from a full core.

3 METHODOLOGY

The materials and methodologies used in this study are described in the following section. They cover the main topics: rock samples, acquisition and processing of NMR experiments and micro-CT, pore network simulation from micro-CT and distributions.

3.1 SAMPLES

The samples considered in this study are a coquina and the limestone Edwards Brown. The coquina sample is originated from the Morro do Chaves Formation, located in Sergipe-Alagoas Basin, Northeast Brazil. According to Hoerlle *et al.* (2018) it is a bioclastic rock, formed mainly by lacustrine bivalves that suffered several processes of diagenesis. The Edwards Brown plugs were acquired at Kockureck Industries and are originated from a layer in the Austin Chalk formation, in Texas, US. They were twin core plugs, one of them of core flooding size (EB_4) and a short core plug (EB_3), which had two slab samples extracted (EB_1 and EB_2) (Figure 12) (Table x). The samples were submitted to three main measurements: routine core analysis (RCA), micro-CT scans at different resolutions, and NMR T_2 and DT_2 . The data of the coquina sample analyzed in this study was a courtesy from Hoerlle *et al.* (2018) and Godoy *et al.* (2019).

Table 1: Rock samples studied, type o data acquisition and dimensions.

Sample	RCA	NMR T_2	Micro-CT	Diameter/L (mm)	Height (mm)
1_34A	x	x	x	36.0	35.3
EB_1			x	25.0	4.0
EB_2			x	12.0	4.0
EB_3	x		x	37.5	13.0
EB_4	x	x		37.2	200.0

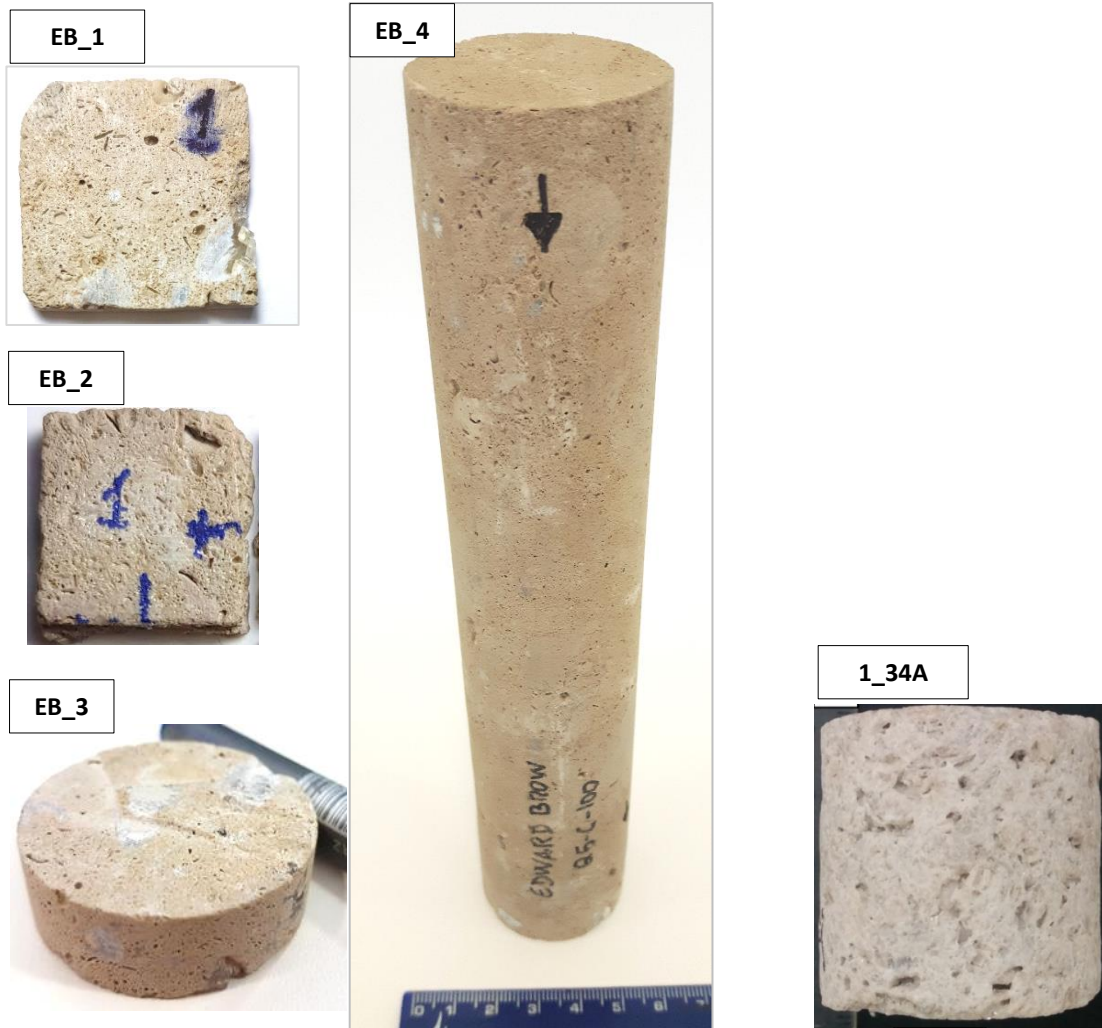


Figure 12: On the left the Edwards Brown samples: EB_1 (slab), EB_2 (1/4 of the slab EB_1), EB_3 (short plug) and EB_4 (long plug); and in the right the Coquina sample 1_34A.

3.2 DATA ACQUISITION

3.2.1 Routine Petrophysics Analysis

3.2.1.1 Porosity and grain density

The methodology used for porosity measurements applies Boyle-Mariotte Law using Helium gas. This methodology considers that the product of pressure versus volume is constant inside a closed system filled with gas, considering constant temperature. The equipment is supported by communicating vases with known volumes. The sample, with total volume V_{sample} , is inserted inside of one of this two vases (core-holder) of volume

V_1 . Gas is injected into the second vase with volume V_2 , confined at known pressure (P_2). Inside the other vase is expanded to the core-holder. The gas is expanded from the second vase to the core-holder and the final pressure (P_f) of the system is measured. The system equilibrium equation is then defined by:

$$P_i V_i = P_f V_f \quad (3.1)$$

Where,

$$P_i V_i = P_2 V_2 \quad (3.2)$$

And,

$$P_f V_f = P_f (V_1 + V_2 - V_g) \quad (3.3)$$

Thus,

$$V_g = V_1 + V_2 - \frac{P_2 V_2}{P_f} \quad (3.4)$$

Finally,

$$\phi = 100 \times \left(\frac{V_{sample} - V_g}{V_{sample}} \right) \quad (3.5)$$

Where V_g is the grains volume of the sample.

The grain density ρ_g is given by the ratio of sample mass weighted and volume V_g .

3.2.1.2 Permeability

The permeability experiment was performed in a nitrogen steady-state gas permeameter. The experiment occurs at moderate confining pressure and steady-state flow rate across the core plug sample. In this experiment, the core plug was placed inside a coreholder with an inlet and outlet region and the gas flow occurs to a differential pressure set between the inlet and outlet. The pressure by which the gas is injected at the inlet and produced in the outlet were monitored and the gas flow rate is measured by a flow meter. Knowing the sample dimensions, fluid viscosity, differential pressure and flow rate, the permeability was calculated using Darcy's Equation (Equation 2.2).

3.2.2 Micro-CT Images Acquisition

The images acquisition was performed in collaboration with the Laboratory of Nuclear Instruments (LIN) at UFRJ. The equipment used to the acquisition was SkyScan 1173, a high energy micro-CT scanner for dense objects (Bruker). The x-Ray source was operating with a current of approximately 133 μ A and 60 kV and it was used a flat aluminum filter of 1 mm. In this acquisition process, the x-rays source is stationary, and the samples are placed in a rotating core holder, which rotated 360° at steps of 0.5° during the acquisition. The images reconstruction was also performed by LIN using the software package NRecon version 1.6.9.4. The total time for scanning the reconstruction of each sample is described in the table below.

Table 2: Samples acquisition and reconstruction time.

Sample	Resolution (μ m)	Acquisition time (hr:min:s)	Reconstruction time (s)
EB_1	12.46	01:25:27	1806
EB_2	7.123	01:12:26	13292
EB_3	17.81	01:25:27	719
EB_3	12.11	02:46:26	8272
1_34A	18.16	01:39:40	1009

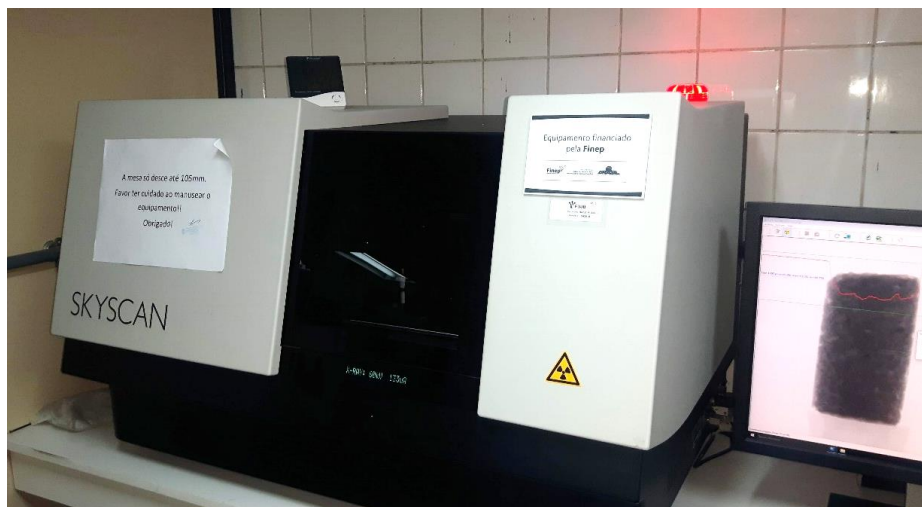


Figure 13: CT Scanner SkyScan 1173 at LIN/UFRJ.

3.2.3 NMR Experiments

For the NMR experiments the Edwards Brown samples were saturated with a brine prepared at LRAP facilities. The brine presented a salt concentration of 30 kppm of KCl, which is indicated for carbonate rock samples that may carry traces of shale (private communication with Souza, 2018). The samples were saturated at a confining pressure of 500 psi to ensure that all pores were filled by the brine.

The NMR experiments were performed by the laboratory UFFLAR, located at the Universidade Federal Fluminense. The equipment used in the NMR acquisition was the low field Maran Ultra (Oxford Instruments, UK) with resonance frequency of 2MHz for each hydrogen ^1H isotope, with magnetic field of approximately 0,047 T (Tesla). The NMR T_2 experiment was performed on the sample EB_4. The focal space of the equipment covers approximately 6 cm, considering EB_4 was a 20 cm length sample, two T_2 experiments were performed, one in the top and other at the bottom of the sample. A DT_2 experiment of this sample was also performed, but due to the relation of sample size larger than the equipment focus, the decay presented a high noise, producing artifacts on the results, and it could not be used in this study.

3.3 NMR PROCESSING

The T_2 results were inverted applying the software FLI (Fast Laplace Inversion) developed in MatLab by Schlumberger-Doll Research Center. As described in section 2.5, this methodology calculated the inverse Laplace transforms of de magnetization decay for T_2 by applying Tikhonov regularization to the inversion stabilization. The T_2 transversal relaxation time were plotted against porosity increment. Due to the challenges encountered in the equipment limitations regarding the investigation coverage of 6 cm and large sample size, the surface relaxivity, parameter used in DT_2 inversion could not be obtained.

3.3.1 NMR T_2 Pore Size Curves

The T_2 curves for the EB sample were normalized to the porosity measured in the section 3.2.1. The coquina sample curve was already normalized to porosity. Both

samples T_2 curves were converted to pore size (radius) by applying equation 2.10. The values considered for surface relaxivity for the samples were:

Table 3: Rock samples surface relaxivity.

Sample	Surface Relaxivity (ρ_2) ($\mu\text{m/s}$)
Edwards Brown	~15
Coquina	35.7

The value for surface relaxivity for the coquina was adopted after Luna *et al.* (2016). The EB surface relaxivity could not be obtained in the experiment, therefore, the value of approximately 15 was adopted as an averaged value based on carbonate rocks measurements presented by Souza *et al.* (2016) and private communication with Boyd (2019). Souza *et al.* presented measurements for 10 different carbonate types. The ρ_2 values presented were tested against the methodology described in section 2.8 for two existents micro-CT resolutions, 17.8 and 12.5 μm , and the maximum porosity for these images resolution was calculated. Surface relaxivity values that reflected in not possible porosity estimations were excluded from estimated average of ρ_2 for Edwards Brown.

NMR T_2 pore size curves were used in the next section, 3.4, as input for threshold selection for image segmentation. As mentioned in section 2.5, if we assume pores having a spherical geometry, and if the minimum pore the micro-CT image can identify is of the size of one voxel, the smallest pore that the micro-CT can identify has the diameter of that voxel size. Considering that, the micro-CT is able to identify up the porosity correspondent to equal or larger than those pore sizes. Therefore, the porosity expected to be estimated by the certain voxel size is represented here as the sum of porosity increment above the truncated (at micro-CT resolution) T_2 pore-size distribution.

$$\phi_{micro-CT,i} = \sum \phi_{increment}(r), \quad for \ r \geq i/2 \quad (3.6)$$

Where $\phi_{micro-CT,i}$ represents the porosity fraction estimated by the i image resolution, $\phi_{increment}$ the porosity increment at each pore radius, and r the radius of the pore.

3.4 MICRO-CT IMAGES PROCESSING

3.4.1 Pre-Processing

The micro-CT images were processed using the software package Avizo 9.5 (2018). First, the images sequence for each sample was imported and stacked in Avizo using the option “Read Complete Volume into Memory”. The images were all imported considering a voxel size of 1 μ m. This configuration helped to avoid miscalculations, and later, the data analyzed in Avizo is converted back to its original pixel size with codes in Mathematica.

In sequence, the images were filtered using the Non-Local Mean algorithm, which denoise them in the XY plane inside a search window. This algorithm compares the neighborhoods voxels of the set search window in order to determine the new value of the current voxel and they are given different weights applying a Gauss kernel to the similar values (Avizo 9.5, 2018). Its use is beneficial since it smooths the high frequency noise without losing borders information, which we use for the definition between matrix and pore regions.

3.4.2 Region of Interest

Following, the processing was continued with the region of interest selection (ROI). The samples scanned were positioned with certain small angles inside the scanner, and due to this fact, extracting a simple square was not effective. The tool Volume edit was applied to select a box inclined with certain angle for the slabs, and a cylinder for the plugs. Therefore, it was possible to preserve the largest volume of the sample to be studied. The area outside the sample was cropped and attributed as grey value of 255. The presence of heavy mineral, which might present a grey value of 255, was neglected for this study when quantifying porosity due to the minimum percentage of 255 tone in the original images.

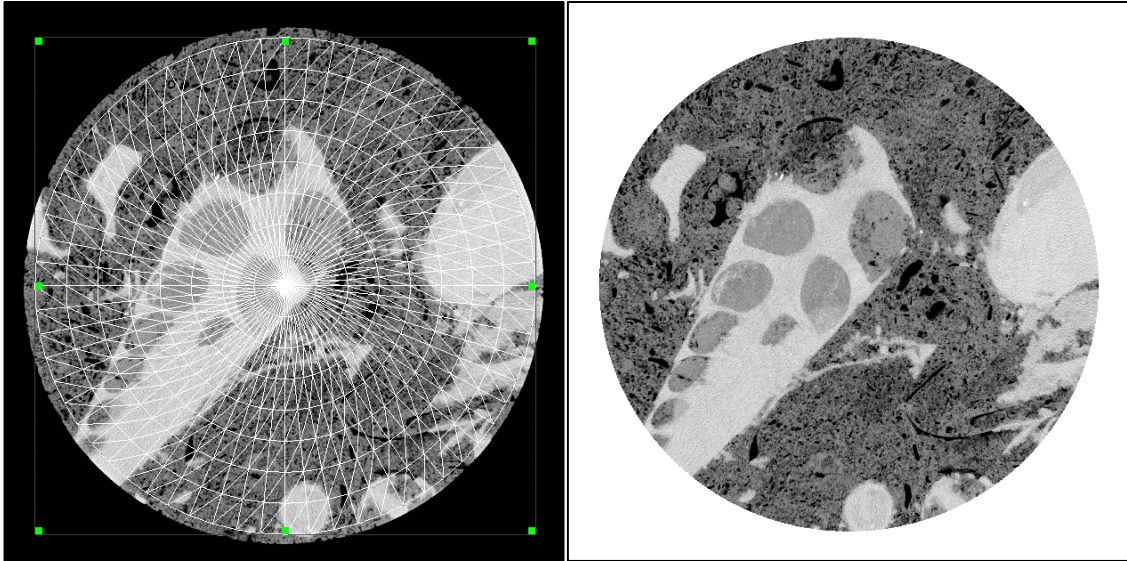


Figure 14: a) ROI selection with Volume Edit tool; b) Cropped region.

3.4.3 Segmentation

Next step was the segmentation. There were analyzed three methodologies for segmentation threshold selection: manual, Otsu's algorithm and NMR guided. The tool Multi-threshold was used as method of segmentation for porosity calculation, where three regions were selected: pore space, rock matrix and exterior area (Figure 15c). For all methods of threshold selection, the pore space was considered as grey values between 0 and x , rock matrix as the range $x - 254$, and exterior region was represented by grey color of 255.

The manual threshold selection is performed by user visual interpretation. The visualization for threshold selection was done by using the tool Interactive threshold, which allows a simultaneous visualization of the area segmented according to the value selected (Figure 15b).

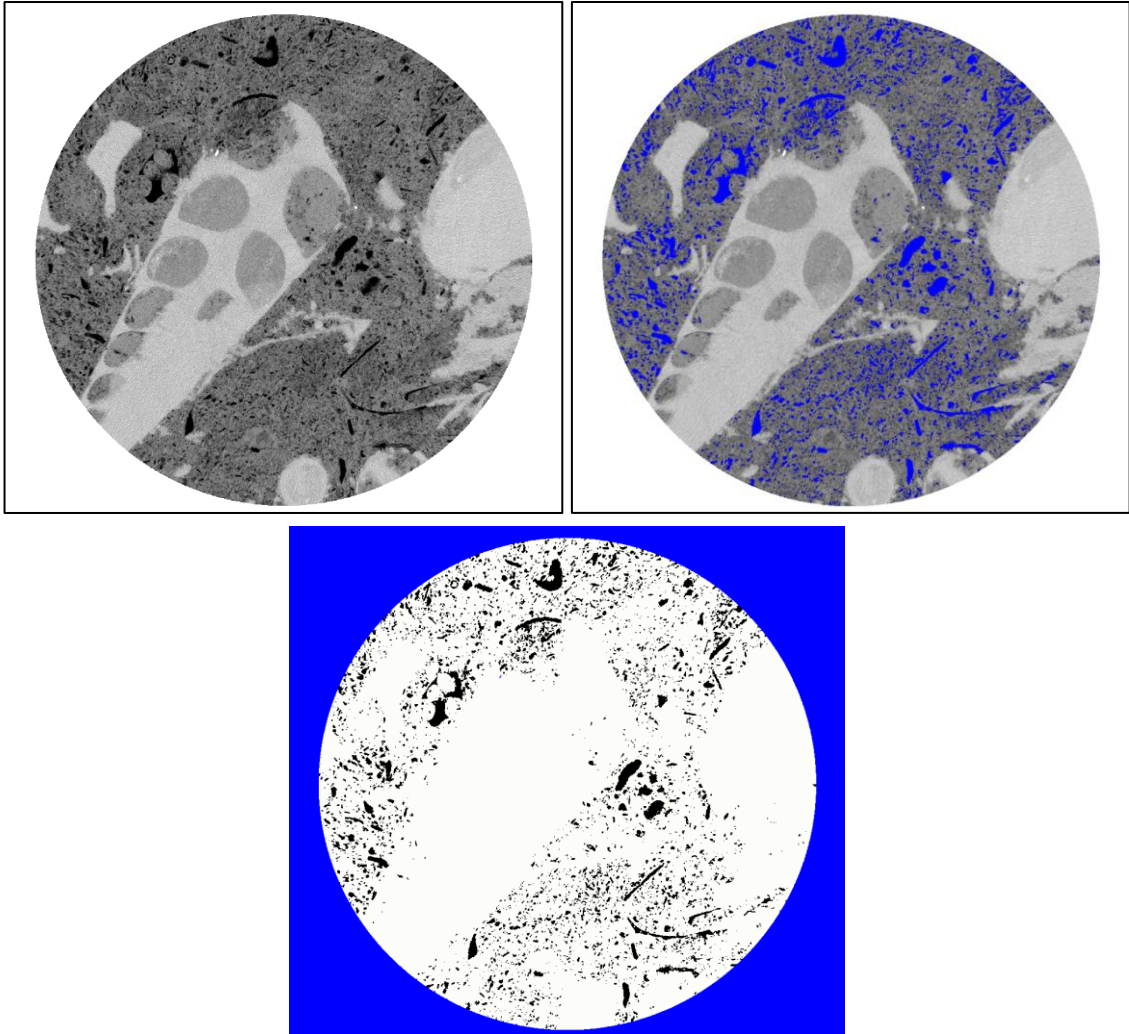


Figure 15: a) Original image; b) Segmented space visualization using Interactive Threshold; c) Segmented image in pore space (black), rock matrix (white) and exterior region (blue).

For applying the Otsu's algorithm for automatic thresholding, the tool Auto-threshold was used. The method factorization was applied, and the tool was run. The outputs of this process were an info file containing the selection parameters and a labeled image.

For the NMR guided threshold selection, only the tool Multi-threshold was used, and the threshold was varied until the resultant porosity was equal or less than the maximum porosity expected. This maximum porosity is relative to pores diameter equal or higher than the pixel resolution calculated from NMR pore size distribution.

3.4.4 Three-Dimensional Digital Rock Model

The three-dimensional digital rock reconstruction and visualization were made by stacking the series of 2D slices of the micro-CT images and attaching a volume rendering or a generate surface tool. This enabled the analyses and visualization of the digital rock model in three main stages: raw image visualization, segmented rock model, pore space or connected pore space visualization.

3.4.5 Porosity

After segmentation we extracted the statistical information using the tool Material Statistics. One of the outputs of this tool was the count number for each of the segmented phase. On the previous section, the images were segmented using the tool Multi-threshold in pore fraction, matrix fraction and exterior fraction. Considering the number of pixels counted in the pore region (N_p) and the total number of pixels of the sample bulk volume (N_t), that are the sum of the pixels from the pore and matrix regions, the porosity was calculated (Eq. 3.7). The porosity estimated in this methodology considered the pores above image resolution, which are mostly formed by meso and macropores.

$$\Phi = \frac{N_p}{N_t}, \quad \text{where } N_t = N_p + N_m \quad (3.7)$$

3.4.6 Micro-CT Pore Network Modeling

After a proper and calibrated segmentation to meet the porosity value according to the NMR pore size curve, a methodology to extract a pore network was performed in the segmented pore space. From the methodologies presented at section 3.4.2, the labeled image generated from the Interactive Threshold method was used as input for the PNM generation.

To characterize the pore space and identify the connected pores, the module Connected components was applied. In the case of the segmented image, this tool ran a search vector to identify adjacent voxels under the same label in the entire 3D image volume and clustered them. In the module configuration the minimum size of voxels

connected was defined. For most cases, a minimum of points around 100 or 1000 was selected. Usually this voxels clusters are not connected to the pore system or form a pore system that is connected from top to bottom of the sample, and will not affect permeability results, and therefore can be excluded. For the plug samples models, only the larger connected pore space was selected due to the computational limitations. Additionally, if a same pore space is characterized with voxel sizes of 20 μm and 10 μm , the latter will present double numbers of voxels for characterizing the same area, consequently, for higher resolution images, the lower limit of pore can be increased without substantial losses of the connected pore space.

After identified the lower limit of connected space, a following labeled image was generated and the tool Auto-Skeleton was connected to it. The tool Auto-Skeleton applied the methodology Maximal-balls, described in section 2.4, to skeletonize the connected pore space in discrete geometries: pores and throats. This module extracted the centerline of filamentous structures from a labeled image data. First, it calculated a distance map of the segmented image, then performed a thinning of the label field such that a string of connected voxels remains. The voxel skeleton is then converted to a Spatial Graph object, which is visually represented by connected lines (Avizo 9.5, 2018). The skeleton generated is classified in nodes, points and segments, which represent voxels, pores and throats respectively.

The data of the pore space skeleton was then exported as .xml files. The files exported contained information of every connection of the skeleton. First, it presented the nodes information: node identification, coordinates, and coordination number. Second the points information for point identification, thickness and coordination. And last, segments information of identification for segment, two nodes that it was connected and all the points connected that compose the segment. Every “ball” defined by the algorithm is also a point, but it is classified as a node (pore), the set of “balls” connecting two nodes plus the nodes itself are classified as a segment, yet, a node can be connected in multiple segments to other pores or even to the same pore.

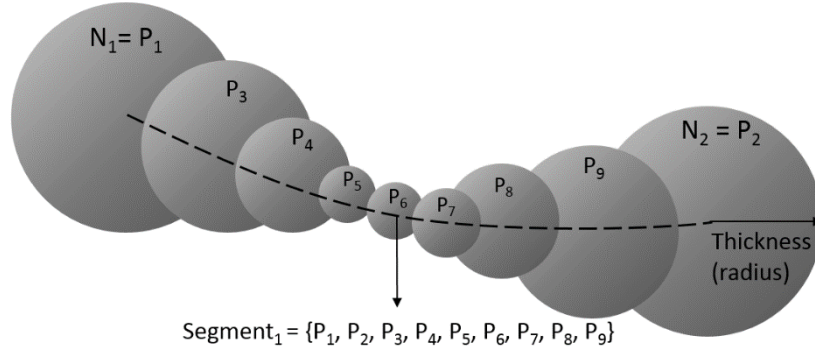


Figure 16: Maximal balls representation of the throats connects two pores (N_1 and N_2)

The skeleton information extracted was processed by codes, and transformed to PNM in PoreFlow, which were represented by the geometries of spheres (pores) and cylinder (throats). A Mathematica code was applied to process it and generate the input files for PoreFlow. It first, imported all the skeleton data described before, and merged its scalar size of the to the original image voxel size, which was set to $1\mu\text{m}$ as described in section 3.4. This code generated the input files for PNM generation in PoreFlow, for throat length (PIPEL), throat radius (PIPER), pore radius (PORER), pore locations (PORE_LOC), pore connections (CONF) and boundary conditions for pores that were used and inlet and outlet for the fluid flow simulations (PORE_INLET). This code also performed two major modifications in the PNM structure, which will be discussed in the next 3 paragraphs.

The skeleton extracted in Avizo was composed by spheres representing both pores and throats. For matters of simplification of fluid flow simulations and for adaptation to PoreFlow, the throats geometry was modified to cylinders. To calculate the length of the cylinder connecting two pores the Euclidean Distance between the center of the two pores connected was calculated according to equation x.

$$d_{P_1P_2} = \sqrt{(x_2 - x_1)^2 + (y_2 - y_1)^2 + (z_2 - z_1)^2} \quad (3.8)$$

Where x , y and z denote the points coordinates in a cartesian system.

To calculate the cylinder radius, which represented the sum of the spheres connecting the pores, an average of their radius was considered. Three different averages were considered: arithmetic, geometric and harmonic (Figure 17).

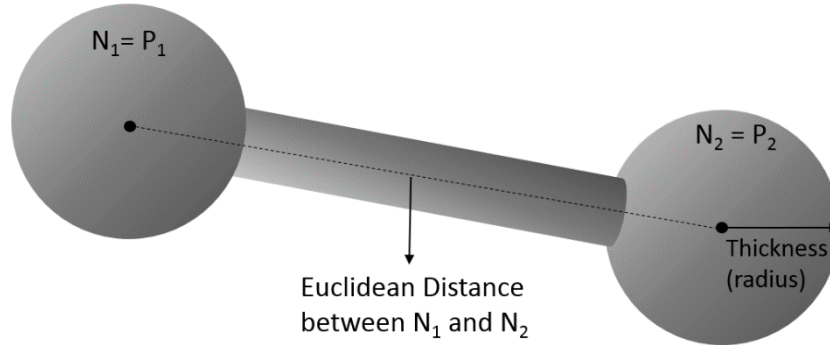


Figure 17: Representation of the network conversion from the maximal-balls geometry to represent the throats from spheres to cylinder.

Additionally, duplicated inverse segments, segments that start and end at same pore body, and segments that connect the same two pore bodies were deleted (Figure 18), because these segments do not contribute to the total permeability.

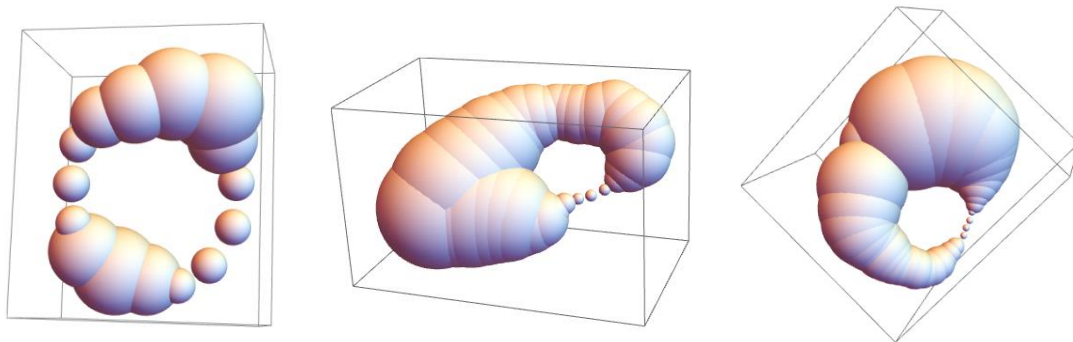


Figure 18: Segments connecting the same pore-bodies that were excluded from the PNM.

Finally, the data was processed and imported in PoreFlow for PNM generation and flow simulation for permeability estimation.

3.4.6.1 Statistical Processing

A statistical study was conducted in order to calculate the probability distributions functions (PDF) of each component from the rock networks extracted. A code in Matlab was used to import, histogram plotting and PDF fitting the data for pore coordination

number, pore radius and throat radius and length. The logarithmic distributed variables of pore radius, throat radius, throat length were analyzed as log of the variable in order to fit normal distributions. The final average coordination number from PoreFlow PNM simulation, which excluded any not-connected throat/pore, was also analyzed.

3.4.7 Fluid Flow Simulation and Permeability

The pore network models were submitted to single-phase fluid flow simulation according to the process described in section 2.4. Fluid flow was modeled in the same direction as the lab measurements (z) for further comparison of permeability results. The fluid presented properties of water with viscosity of 1 Centipoise and density of 1000 Kg/m³. PoreFlow calculated the fluid flow between each pore and permeability was calculated as an average of the final fluid flow in the PNM over the whole sample volume. The permeability was calculated after achieving a constant flow rate by applying Darcy's Equation (Eq. 2.8). PoreFlow also calculates the porosity of the PNM, which is based on the ratio of the PNM pore space volume divided by the volume of a square sample, that represents its bulk volume. The square sample size is calculated based on the minimum and maximum PNM elements coordinates in (i, j, k) .

3.5 REV

For the REV study the samples were divided according to Figure 19. First, the core plug samples were processed according to the sections 3.3.1 and 3.4, then subsamples were extracted following the order:

1. Q, maximum inscribed square,
2. P1 and P2, partitioning of Q in the XY plane in two parts,
3. Q1 and Q2, partitioning of P1 in two in the XY plane, Q3 and Q4, partitioning of P2 in two in the XY plane,
4. Partitioning of Q1, Q2, Q3, and Q4 in two in the Z direction, forming 8 final subsamples.

The coquina samples were partitioned in all 4 steps mentioned, but the Edwards Brown core plug (EB_3) was partitioned only until the 3rd division due to the sample

small size in Z. The slabs were partitioned from step 1 to 4, where the partition 1 was already its largest value.

All subsamples were processed according to the sections 3.3.1 and 3.4 and the results for porosity and permeability were plotted against sample volume. For porosity, REV was considered for subsamples that did not presented a variation superior do 10% of the largest sample measured.

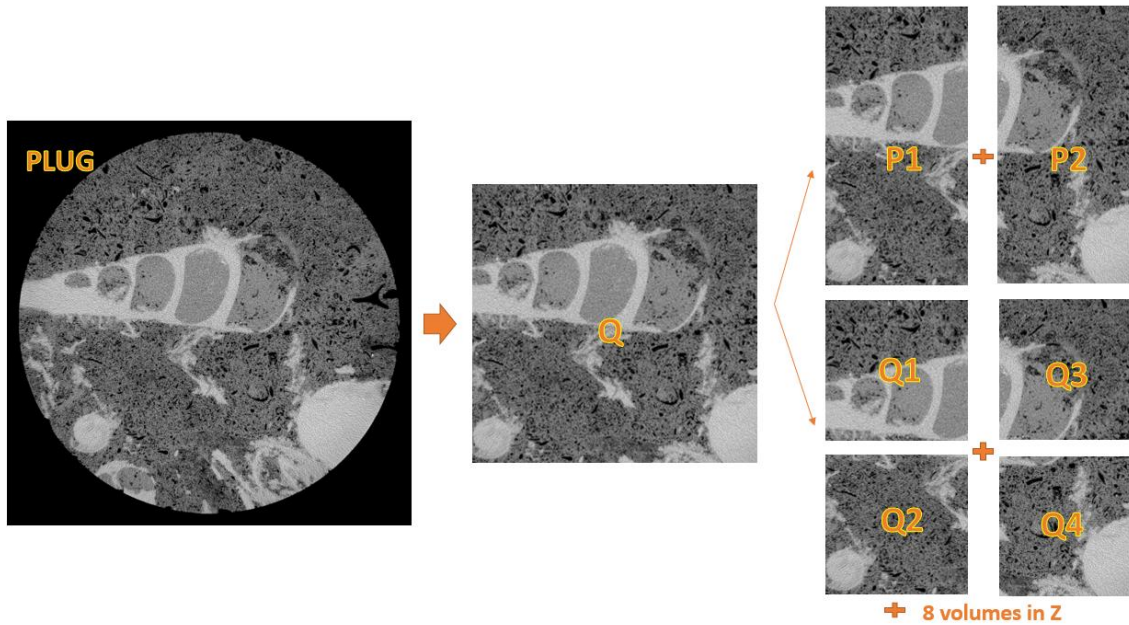


Figure 19: Workflow to crop subsamples from the rock plug for REV study.

Additionally, as reported by Vik *et al.* (2013), the coefficient of variation C_v , was calculated for the samples. C_v is a dimensionless quantitative estimator of heterogeneity. It is defined as the ratio between standard variation of a property and the property arithmetic mean Eq. (3.9).

$$C_v = \frac{\sigma}{\bar{x}} \quad (3.9)$$

If the number of samples is equal or less than 10, a correction factor must be applied:

$$C_v = C_v \times \left[1 + \frac{1}{4(n-1)} \right] \quad (3.10)$$

Where n is the number of samples.

We also analyze permeability heterogeneity according to the proposed classification of C_v from Corbett and Jensen (1992). Where C_v values smaller than 0.5 implies an effectively homogeneous rock, values between 0.5 and 1 implies a heterogenous rock, and values greater than 1.0 represent very heterogeneous rocks.

3.6 SYNTHETIC PNM GENERATION

From the parameters observed in the core plugs simulated in section 3.4.4 synthetic PNM were constructed. The data needed to generate a PNM were: pore and throat radius distribution, throat mean length and final mean coordination number. A module in the software PoreFlow was applied to generate the synthetic PNM.

Poreflow is able to generate a multi-directional pore network that is based on a regular cubic lattice that can simulate PNM geometries for sphere representing pores, and cylinders representing throats. Although limited and fixed connections are expected in lattice-based networks, PoreFlow is able to support up to 26 connections in 13 different directions (Raouf and Hassanizadeh, 2009).

Three approaches for generating a synthetic PNM that was representative to the ones modeled in micro-CT were evaluated. First, we considered the original micro-CT PNM inputs for pore and throat radius. Second, we applied probability distribution functions to generate the pore and throat radius inputs. These probability distribution functions were developed from the micro-CT PNM data. Third, it was used average pore radius extracted from the micro-CT PNM and probability distribution functions to generate the pore throat radius distribution.

In PoreFlow, the distribution assigned for pore and throats are randomly placed, but as a lattice network, only a constant distance between pore centers could be considered. When a network was created, the first parameter evaluated in comparison with the statistics from the micro-CT PNM was the final coordination number. Following, sample dimensions, average distance between pores centers (N_{cont}), number of pore and throats in the sample volume. Last, we checked final values of porosity and permeability.

4 RESULTS AND DISCUSSION

4.1 DATA ACQUISITION

4.1.1 Routine Petrophysics Analysis

The results from routine core analysis are shown in Table 4. The measured results were further used in this dissertation for comparison with the values for porosity and permeability estimated from the micro-CT images. According to Kurotori *et al.* (2018) Edwards Brown samples present microporosity, which can be observed comparing the results from the coquina 1_34A and EB for porosity-permeability ratio and further presented results for micro-CT images and NMR pore-size distribution.

The Edwards Brown samples presented a high value for porosity, between 31.4 and 33.6%, but did not present a very high permeability (~300mD). This indicates that its networks were not well connected as the coquina sample 1_34A, or that its connection quality was decreased as a result of the microporosity. The coquina sample presented a medium value of porosity (16.3%) while presented almost the double of EB permeability (639 mD).

Table 4: RCA for samples studied.

Sample	Porosity (%)	Permeability (mD)
1_34A	16.3	639.0
EB_2	31.4	314.4
EB_3	33.6	265.6

4.1.2 Micro-CT Images Acquisition

Table 5 presents the information for each image acquisition of the samples for: number of slices, pixel size and total file size.

Table 5: Samples micro-CT number of images and resolution.

Sample	Number of Slices	Resolution (μm)
EB_1	2236	12.46
EB_2	2112	7.123
EB_3	963	17.81
EB_3	1504	12.11
1_34A	2210	18.16

4.1.3 NMR Acquisition and Processing

The NMR T_2 curves acquired for the coquina (Hoerlle *et al.*, 2017) and the two Edwards are presented Figures 20, 21 and 22. The coquina sample 1_34A show two strong modes and a smaller one. The multimodality in T_2 curves representing multiple pore systems are common in carbonate rocks because they usually present pore generated from different rock formation processes. Wetsphal *et al.* (2005) affirms that there is a reorganization of primary rock formation porosity during diagenesis.

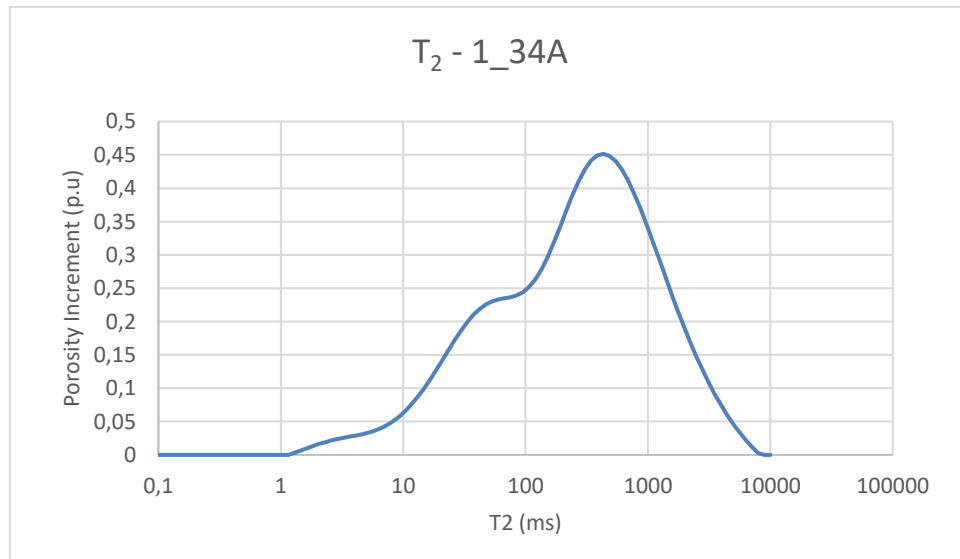


Figure 20: NMR T_2 curve for the sample 1_34A.

The T_2 measurements for the Edwards Brown of 20 centimeters of length present a strong coherency of shape. In comparison with the coquina, this sample presents only

one strong mode and a second smaller one. This may represent a smaller degree of heterogeneity of the pore space if compared to the coquina sample. Additionally, as referred in the section 2.5, larger pores result in large decays times. Considering that, the EB T_2 curves reach its maximum around 1100 μs and present smaller pores if compared to the coquina sample, that reached its maximum T_2 in approximately 10000 μs .

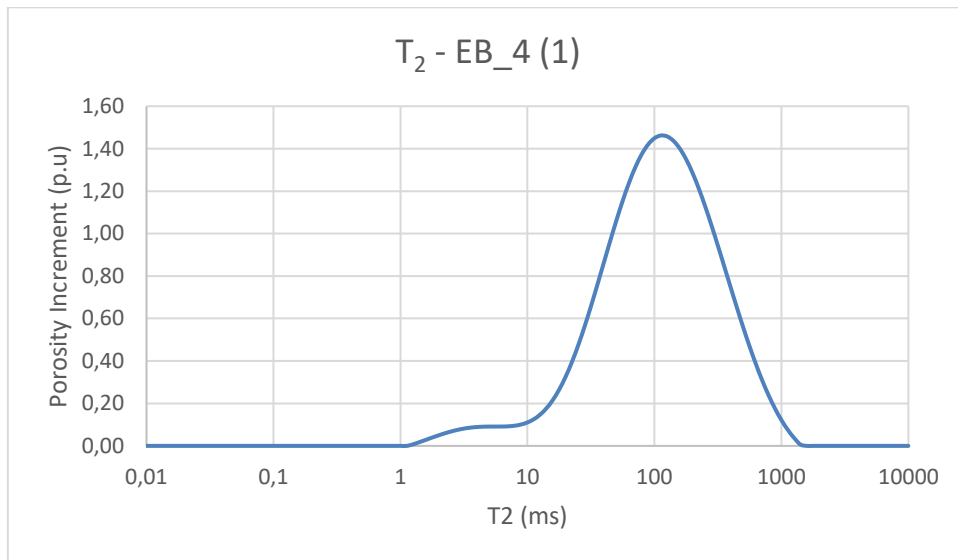


Figure 21: NMR T_2 curve for the sample EB_4, 1st measurement.

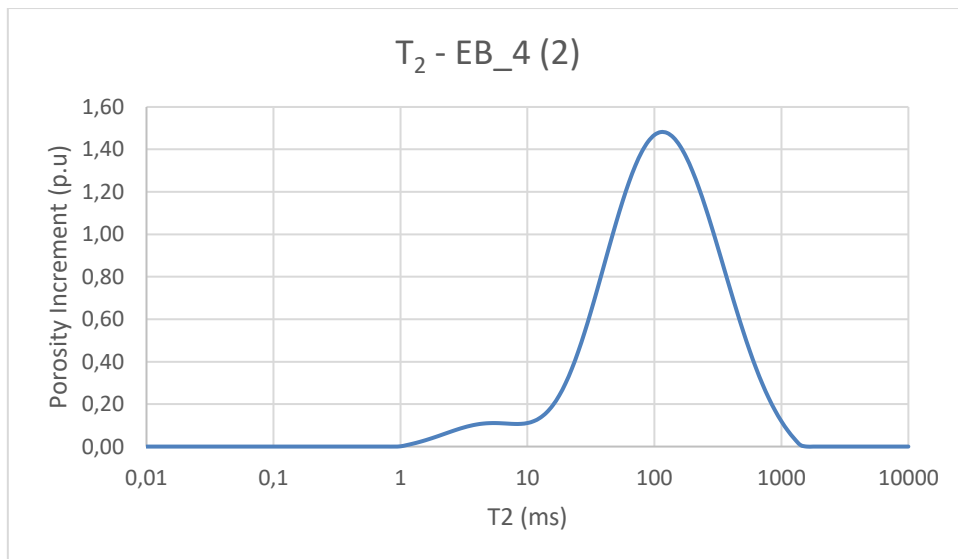


Figure 22: NMR T_2 curve for the sample EB_4, 2nd measurement.

For the determination of the ρ_2 , value used to convert the T_2 curve to pore radius, 10 measurements of ρ_2 for diverse carbonates rocks were considered. Each rock value of ρ_2 was applied to the T_2 conversion, and the consecutive maximum values of porosity expected for the EB micro-CT images of 17.8 and 12.5 μm were calculated considering the measurement EB_3 (1) (Table 6).

The ρ_2 values that resulted in maximum porosity lower than 8% for the micro-CT resolution of 12.5 μm were discarded because they would suggest that is only possible to estimate approximately 25% of the total porosity the rock ($\phi_{lab} = 31.4\%$), even considering a high resolution images, the same criteria was applied to the largest ρ_2 value from the table. Additionally, as discussed with Boyd (private communication, 2019), carbonates usually range between 5 and 15. Finally, the average surface relaxivity of the samples in bold in the table below was used as an approximation, which may consider a variance, to convert the T_2 pore-size distribution. As result, the maximum porosity observed in the EB image samples of approximately 12.5 μm is 14.25%, while for the images with resolution of 17.8 μm the maximum porosity expected is 10%.

Table 6: Rock samples analyzed for surface relaxivity and maximum porosity evaluated for micro-CT resolutions.

Sample	Φ_{lab} (%)	K_{lab} (mD)	ρ_2 ($\mu\text{m/s}$)	Φ_{CT} (EB CT- res. 17.8 μm)	Φ_{CT} (EB CT- res. 12.5 μm)
Indiana 8-10 mD	9.1	0.4	2.9	0.00%	0.53%
Indiana 2-4 mD	13.8	1.9	3.3	0.12%	0.84%
Winsconsin	5.6	0.8	8.6	4.49%	7.60%
Leuders	16.2	1	10.5	5.44%	10.10%
Sillurian Dolomite	12.4	18.3	9.5	5.44%	8.81%
Guelph Dolomite	7.9	4.3	12.4	7.60%	11.45%
Edwards Yellow	22.9	165	16.5	10.10%	14.29%
Desert Pink	30.5	95.5	18.8	12.85%	17.21%
Austin Chalk	23	10	23.3	14.29%	18.66%
Indiana 70 mD	18.9	301	35.8	20.08%	24.00%
Average (samples in bold)			15.2	10.0%	14.25%

The curves were converted from T_2 in ms (Figure 20 and Figure 21) to length in micron by applying equation 2.10. The surface relaxivity values were assumed as 35.7 and ~ 15 for the coquina and Edwards Brown, respectively. The surface to volume ratio was considered as 3 once it was assumed pore as perfect spheres. The results are plotted in Figure 23 and Figure 24 e 25. The plots are composed of a blue line (real data) and the red dotted line, that represents the portion of porosity that can be visualized by the images of $18.16\mu\text{m}$ (1_34A) and $17.81\mu\text{m}$ (EB_4), considering that the minimum pixel size is equivalent to the minimum pore diameter that can be observed by that image. The results of the threshold value estimated according to the NMR pore-size distribution will be discussed in the next section.

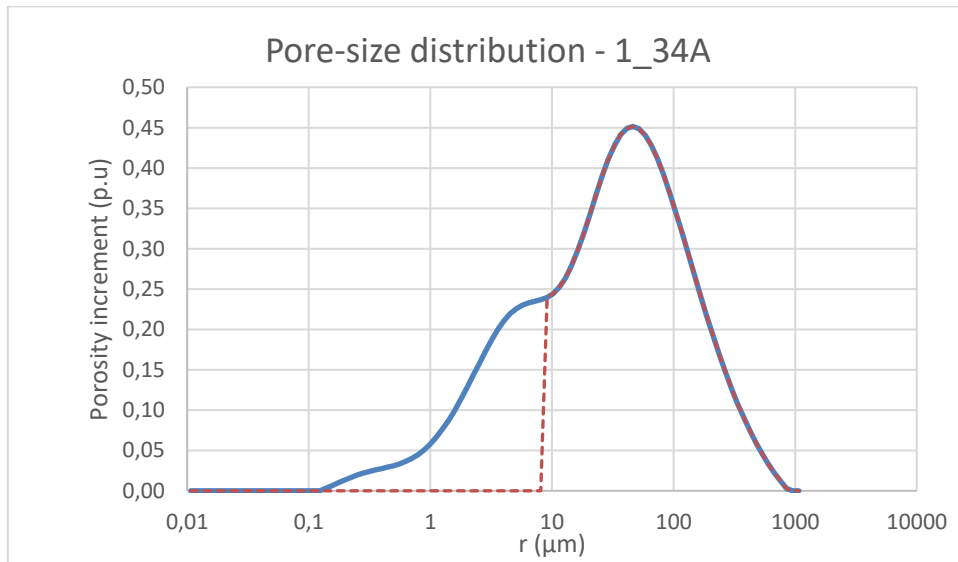


Figure 23: NMR T_2 pore size distribution curve for the sample 1_34A (blue line) and fraction of the curve that can be observed from the micro-CT image at resolution of $18.16\mu\text{m}$ (dashed red line).

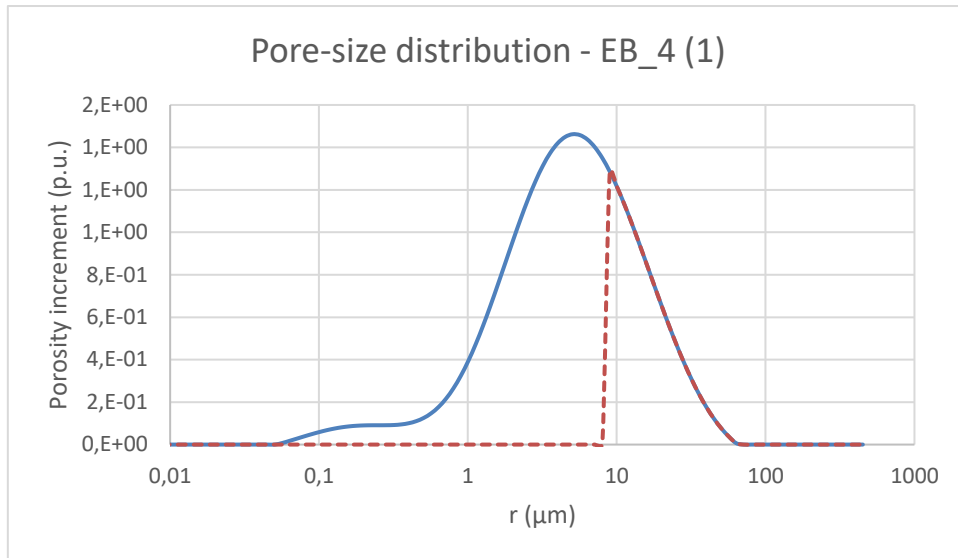


Figure 24: NMR T_2 pore size distribution curve for the sample EB-4 (1st measurement) in the blue line and fraction of the curve that can be observed from the micro-CT image at resolution of $17.81\mu\text{m}$ in the dashed red line.

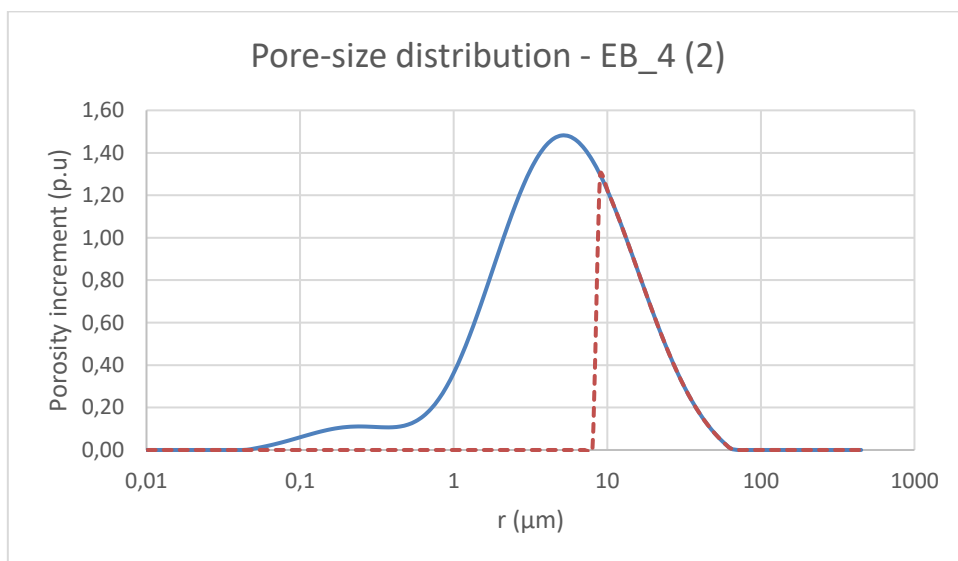


Figure 25: NMR T_2 pore size distribution curve for the sample EB-4 (2nd measurement) in the blue line and fraction of the curve that can be observed from the micro-CT image at resolution of $17.81\mu\text{m}$ in the dashed red line.

The Edwards Brown T_2 measurements show a great consistency. For example, the maximum porosity calculated for images of $17.81\mu\text{m}$ was 10.06 and 10.10 % for experiment (1) and (2) respectively, which represents a difference of less than 0.1%.

Therefore, only the results from measurement (1) were used in this work. This also indicates a good degree of homogeneity of the patterns found in this rock.

Finally, the table below show the results of maximum porosity of each micro-CT resolution used in this study. As observed in the T_2 curves, the EB samples present smaller pores in comparison with the coquina. Therefore, considering approximately a micro-CT resolution of 18 microns, it was possible to identify porosity up to 75% of the coquina sample lab porosity, while for the EB_3 sample it was possible to estimate only 30% of the total lab porosity.

Table 7: Maximum porosity estimated for each micro-CT resolution based on NMR T_2 pore size distribution.

NMR porosity vs. micro-CT maximum porosity @ each resolution			
	Porosity (NMR) (%)	Micro-CT Porosity (%)	Percentage of measured (%)
1_34A	13.96	-	-
1_34A (18.16 μ m)	-	10.44	74.78
EB_3 (measured)	33.6	-	-
EB_1 (17.81 μ m)	-	9.88	29.40
EB_3 (12.5 μ m)	-	14.42	42.91

4.2 MICRO-CT IMAGES PROCESSING

Visually comparing both samples in the micro-CT images (Figure 26), it is possible to identify that, in general, the pores in the EB sample are smaller and in higher quantity, while on the coquina 1_34A sample, pores are likely to be larger and better defined by the images of about the same resolution. The presence of the microporosity may cause to the low permeability to porosity ratio of the EB samples compared to the coquina sample, while EB holds an average of 31-33 % of porosity and maximum of 314 mD of permeability, the coquina sample presents 639 mD of permeability for only 16.4% of porosity. These values show that the pore-network of the coquina sample is better connected than the EB samples. Looking at the perspective of the NRM pore-size distribution, if an average image resolution of 18 microns is assumed for both samples, up to 75% of the total NMR porosity can be analyzed for the coquina, that is, 75% of the

pore diameters are over 18 microns. If the same is considered for the EB sample, only 30% of the pore diameter are over 18 microns.

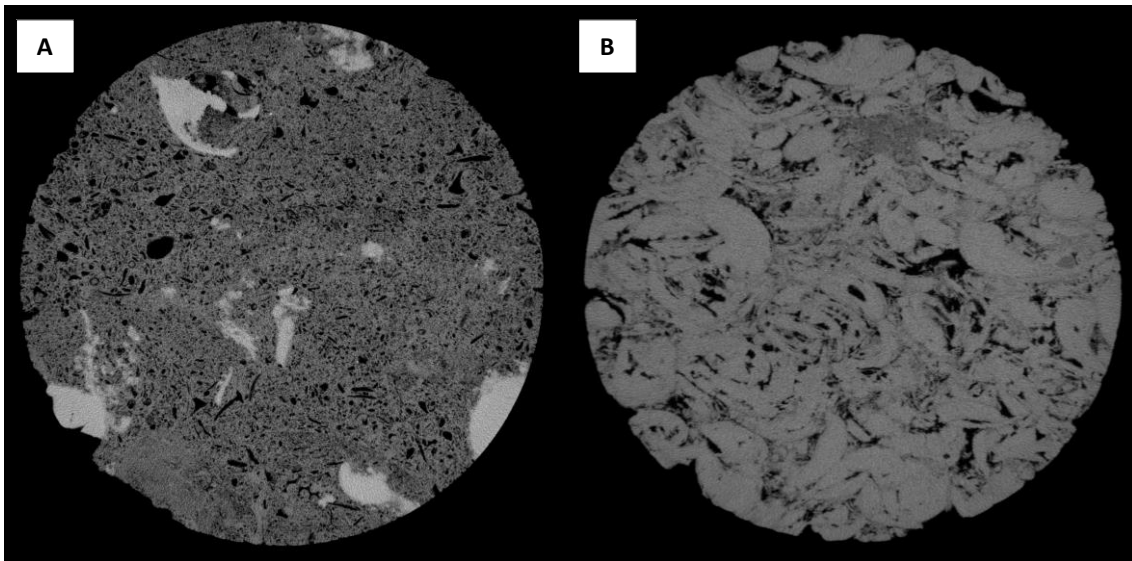


Figure 26: Micro-CT image of: a) EB_3 (18um); and b) 1_34A (18um)

4.2.1 Pre-Processing

The filter Non-Local means (Avizo, 2018) was applied to all micro-CT images for noise correction. After they were loaded in Avizo, the rock region was selected excluding the external part of image for reasons of decreasing the size of data processed and also to dismiss noise zones that may generate artifacts during the correction. The value selected for the search window was kept the software standard of 21 and was not increased due to the cost of computational processing. In figure 27, the result of the filter for the sample EB_3 can be visualized, where the image is smoothed and the borders of the structure are better defined.

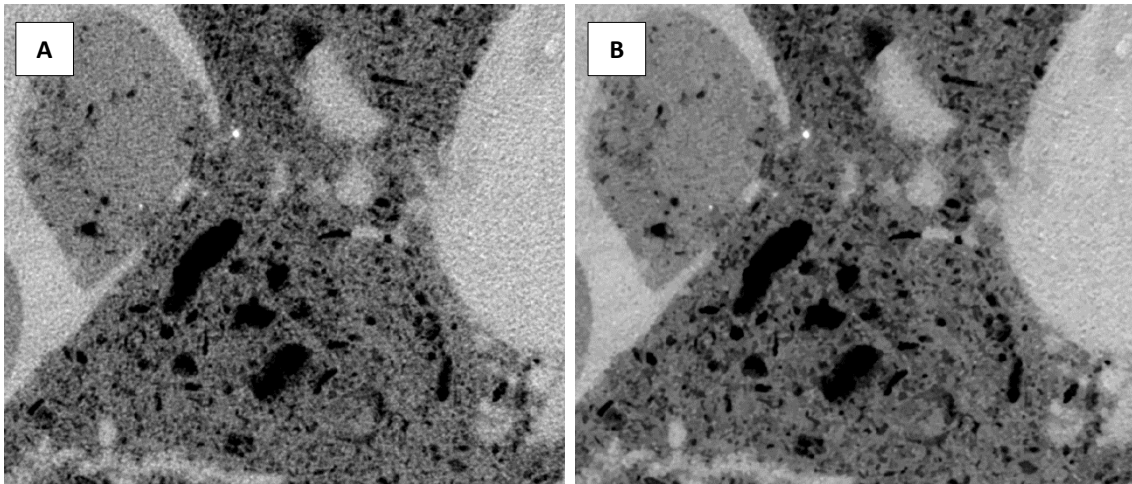


Figure 27: Comparison of raw image (a) and filtered by Non-Local Means (b) of sample EB_3.

4.2.2 Segmentation and Porosity

Three methods for segmentation were applied to the samples' images (Table 5): manual, Otsu's algorithm and NMR threshold. The manual method resulted in the most conservative values for threshold and porosity result represented around 38% and 56% for EB_3 (12.1 μ m) and 1_34A (18.1 μ m) respectively, of the value measured in laboratory. Moreover, in the scenario of the Edwards Brown samples, which were imaged at different resolutions, it is possible to observe the difference of porosity estimated considering the same threshold value. In the case of this sample, the pores above diameter of 12.11 are responsible for a large amount of the total porosity.

The threshold values estimated by Otsu's algorithm reflect to a more optimistic scenario if compared to the manual selection, and also optimistic if compared to NMR thresholds for the samples EB_3 and 1_34A. The porosity values considering the estimated threshold represent 77% for the coquina, and 52% for EB_3, if compared with the lab measurement for the sample EB_3.

Table 8: Thresholds evaluated for images segmentation.

Sample	Resolution (μm)	Threshold (manual)	Threshold (Otsu)	Threshold (NMR)
1_34A	18.16	54	72	64
EB_1	12.46	65	80	-
EB_2	7.12	43	47	-
EB_3	12.11	55	66	62
EB_3	17.81	43	61	57

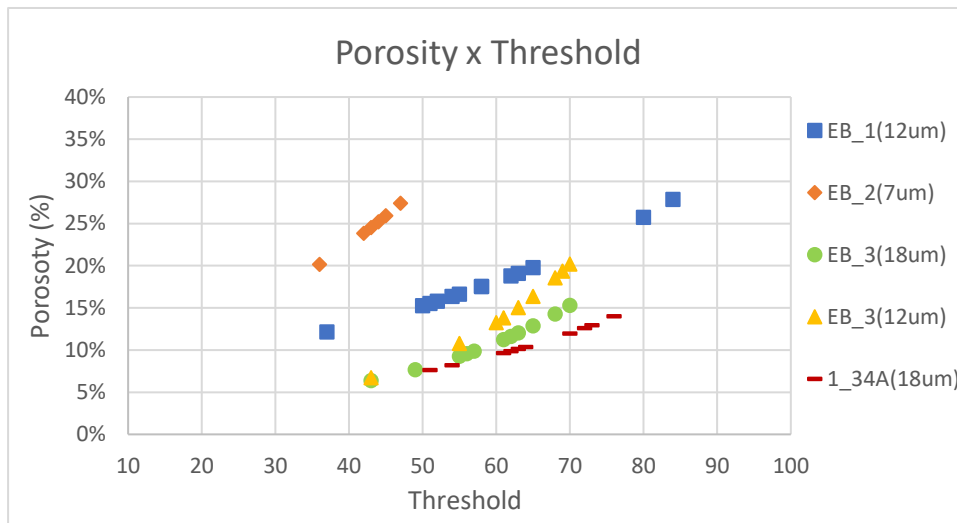


Figure 28: Comparison of the threshold value and resultant porosity estimated from the micro-CT images.

Finally, the threshold value applied to the workflow was determined after the boundaries established by the NMR pore-size distribution. Although the manual selection seems too conservative and the Otsu may be too optimistic, NMR pore-size distribution was able to present a physical measurement to define the segmentation threshold. Table 6 shows in the first column, the total NMR porosity of each sample, and the maximum porosity estimated by the micro-CT image at its resolution. The second column show the threshold value used, and the third column shows the porosity estimated by the micro-CT images. The last column shows the percentual errors calculated between the maximum porosity estimated by the resolution and the final porosity estimated.

Table 9: Comparison of porosities expected at each resolution and result porosity value for threshold.

NMR porosity vs. micro-CT porosity				
	Porosity (NMR) (%)	Threshold	Micro-CT Porosity (%)	Error (%)
1_34A (measured)	13.96	-	-	
1_34A (18.16 μ m)	10.44	64	10.37	0.67
EB_3 (measured)	33.6	-	-	
EB_1 (12.11 μ m)	14.25	62	14.42	0.01
EB_3 (17.81 μ m)	10.0	57	9.88	0.01

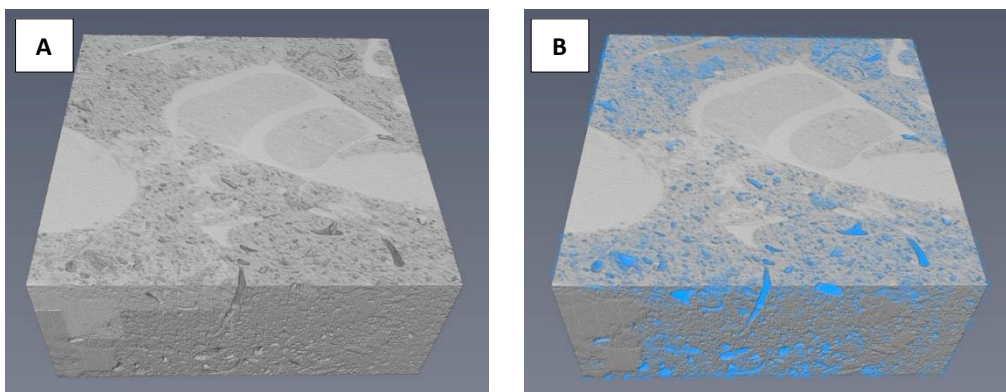


Figure 29: a) 3D rock model and b) pore space segmented model of EB_3.

4.2.3 Micro-CT Pore Network Models

The results for the pore network models are presented in the following sections. First, it is presented the impact of the image resolution on the PNM pore-size distribution. Second, the results of permeability from the fluid flow simulation in the PNMs. Last, the statistics analyzed for the coquina 1_34A and EB_3 plug samples.

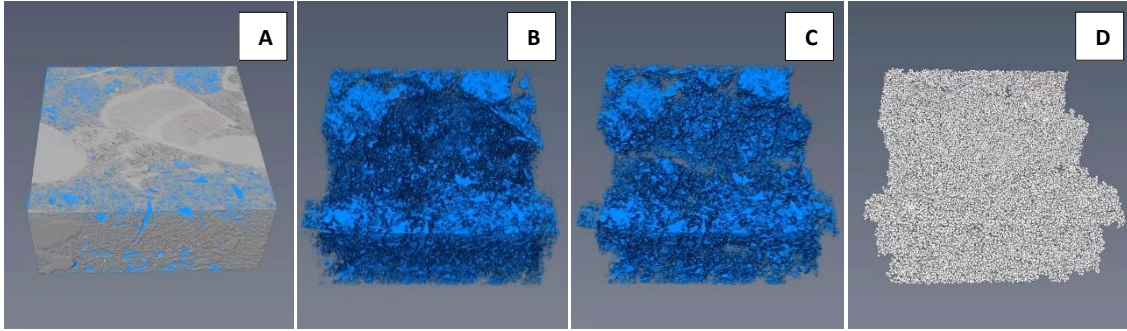


Figure 30: Sample EB_3: a) 3D models of rock sample and connected pore space in blue; b) All pore space segmented; c) Connected pore space; and d) Pore space skeleton.

4.2.4 Fluid Flow Simulation and Permeability Estimation

The single-phase fluid flow simulations and the calculation of the permeability were performed using PoreFlow and applying the methodology described in the section 3.4.7. The software calculates the equations described in section 2.4 as presented by Raouf et. al. (2013).

For the simulation, it was considered a percentage of 2% of the total z length of the sample 1_34A. For the EB plug sample EB_3, the percentage applied was of 1% because the length of the sample was only 10 mm. Moreover, the percentage of 1% was also applied to the modeling of the slab samples EB_1 and EB_2 since they also present a very short length in z of 1.74 mm.

Table 10: Permeability results comparison.

	K lab (mD)	K simulated (mD)		
		arithmetic mean	geometric mean	harmonic mean
EB_1	-	4087.30	2573.50	1627.20
EB_2	-	418.49	279.10	191.61
EB_3 (17.81 um)	314.4	25.55	14.51	7.83
EB_3 (12.11 um)	314.4	221.43	165.88	123.27
1_34A	639	443.40	294.21	166.46

The permeability for the plug samples were obtained with the volume representing the maximum inscribed square in its cylinder volume. This was done because PoreFlow

only considers cuboid shapes, therefore, the results that were obtained for the plugs were underestimated. For the coquina sample 1_34A, the result that best approached the laboratory measurement was applying the arithmetic mean to the calculation of the pore-throats. The lab measurements pointed a value of 639 mD and the simulated 443.3. Considering that at this resolution it is not possible to estimate the pores below resolution, it is expected that both porosity and permeability simulated for this sample present a similar but lower value. The same configuration is expected for the plug samples of EB_3. This rock sample presented the presence of microporosity, therefore image resolution of around 18 μm was not able to resolve the pore space to meet values closer to the lab measurements. On the other hand, the estimative performed for this sample with image resolutions of 12 μm present an approximate result for permeability. The value that best approached the lab measurements was applying the arithmetic mean.

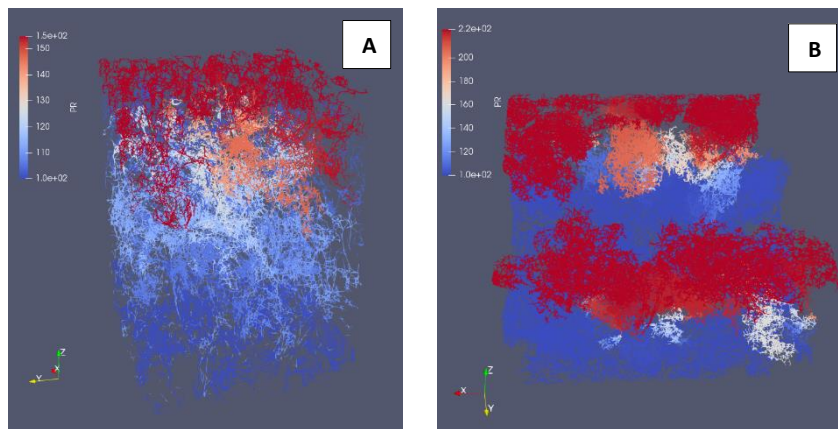


Figure 31: Pore network final pressure gradient during the fluid simulation of a) 1_34A and b) EB_3.

For the slabs samples of EB the results were expected to present a large variance from the lab measurement, since their volume are not considered as a minimum REV volume for permeability. The results for the sample EB_1 presented an order of magnitude higher than the lab measurement. The result that best approached it was applying a harmonic mean to define the throat radius. On the other hand, the sample EB_2, that was imaged at resolution of 7 μm , presented a result approximate to the lab measurement. The resolution of this sample impacted in a better definition of segmentation threshold and characterization of the pore space. Therefore, in this case the resolution was able to highly impact the results. Nonetheless, it is important to notice that

this resolution is impracticable to other more representative volumes because of acquisition equipment limitations and computational costs.

4.2.5 Impact of Micro-CT Resolution on Pore Network Distributions

Two samples were imaged at 2 different resolutions, and in this section the pore radius size, of the generated PNM of each sample is plotted. For the sample EB_1 and EB_2, we adopted the following: the slab EB_1 was imaged with resolution of 12.46 μm , and then, it was divided in 4 subsamples (Figure 32b). The subsample written with “1” was then labeled as EB_2 and was imaged with resolution of 7 μm . The image acquisition of 7 μm could not be performed in the sample EB_1 due to the equipment limitations. For the comparison, we selected the region labelled as 1 of EB_1, correspondent to EB_2. In figure 32, it is possible to note by the yellow arrows the same characteristic is present in all samples, which also possible to observe in the micro-CT scans.

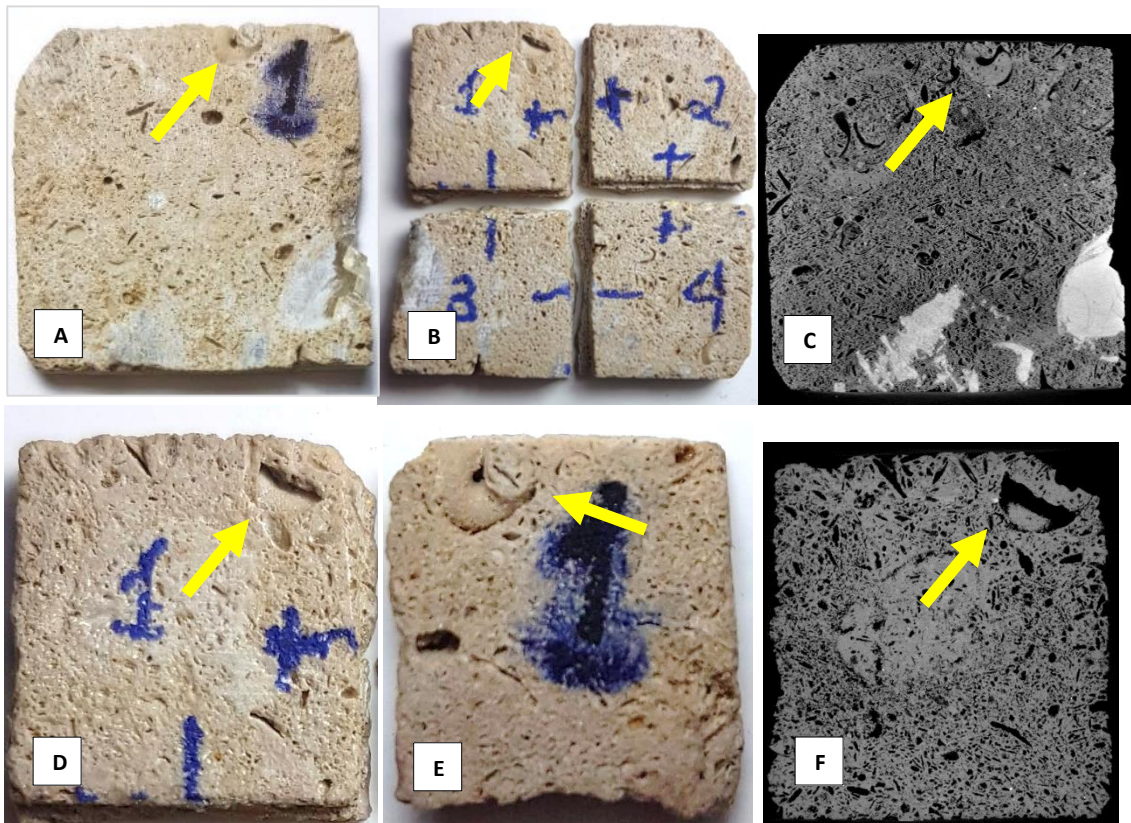


Figure 32: a) EB_1 sample; b) Division in 4 subsamples; c) Micro-CT image of EB_1 with 12.26 μm ; d) Top of subsample EB_2 from EB_1; e) Bottom of subsample EB_2; and f) Micro-CT image of subsample EB_2.

The result of both samples PNM pore radius size distribution (PSD) is shown in figure 33. Both curves show a similar behavior but the sample with 12 μm is a little shifted to the right. Applying the 7 μm micro-CT images we were able to analyze a larger density of pores that were below the $\ln(r) = 2$. An observation in both curves is that the first point presents a peak. This peak represents the radius at the resolution of the sample, and they carry a cumulative noise from the limitation of the resolution. Pores that are below that resolution may still be classified as pores, as well pore slightly higher than the resolution may also be cumulated in this region. This generates the cumulative effect at the beginning of both distributions.

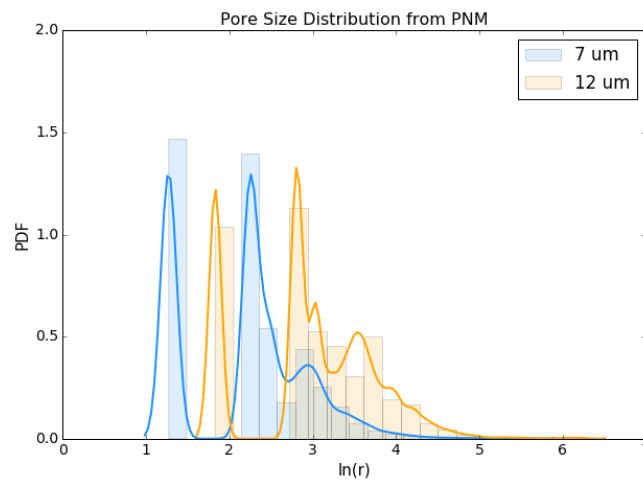


Figure 33: Density plot of the PNM pore size distribution of the same area of sample EB_1 at resolutions of 7 and 12 μm .

The same methodology was applied to the plug sample EB_3. In this case, the lower resolution image was able to estimate a more uniform shape of curve and do not present large peaks as seen in the other scenarios. This also happens because, at this high resolution, and considering the volume of the sample, it was only possible to model the largest connected pore network of the sample, filtering smaller disconnected networks that may increase the first two peaks observed in the curves. On the other hand, all points were considered for the sample with 18 μm . The pores larger than the $\ln(r)$ present a coherence with the observed density of the same sample at 12 μm .

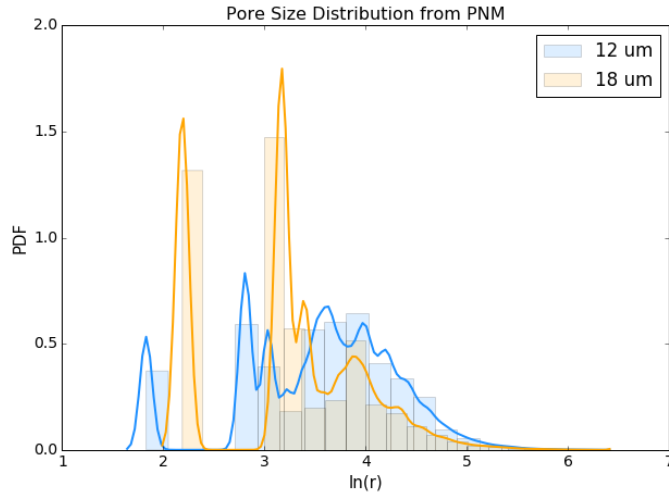


Figure 34: Density plot of EB_3 sample at resolutions of 12 and 18 μm .

4.3 REV ANALYSIS

The following volumes division were adopted for each sample:

Table 11: Subsamples Division volumes in mm^3 .

Sample	Volume in mm^3				
	Plug	Inscribed square (Q)	1 st division (P1/P2)	2 nd division (Q1/Q2/Q3/Q4)	3 rd division (8 volumes in Z)
1_34A	21846	13775	6885	3444	1722
EB_1	-	691	345	173	-
EB_2	9711	6000	3000	1500	-

4.3.1 Porosity REV

The porosity was estimated to a total of 1 sample and 15 subsamples for the coquina 1_34A. The plug was first analyzed, second the maximum square inscribed in its radius. Then, in the XY direction it was divided into other two squares, which were then, divided into other two squares. Ultimately, the four last squares were divided by two in the Z direction. The results for the porosity estimated for each subsample and sample are plotted as a function of sample volume in the Figure 35. From the 15 subsamples analyzed only one presented a percentual variation from the sample higher than 10%. Therefore, considering a confidence percentage 94% percent, samples above approximately 3400 mm^3 can be considered as REV for porosity for the coquina sample 1_34A.

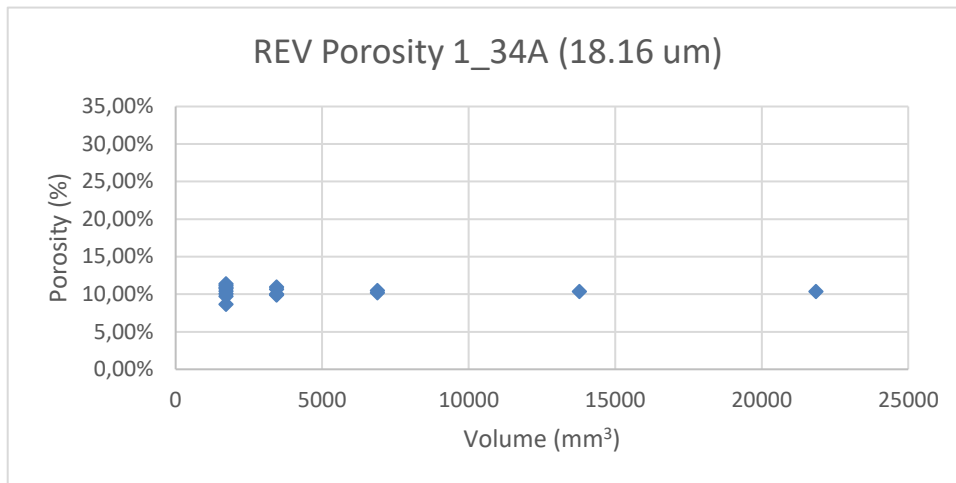


Figure 35: REV analysis for porosity of sample 1_34A.

The table below presents the porosity values measured for all subsamples, the absolute and relative error considering the plug measurement. Moreover, it presents the arithmetic mean, standard deviation and the coefficient of variation C_v . These last 3 parameters were measured considering the sample of same volume and above. Therefore, they present a cumulative result of increasing the subsamples. The data presented in this table is also supports that the REV for porosity to be considered for samples above 3400 mm^3 , where the arithmetic mean of all measurements reflects the plug porosity (10.4% and $\text{STD} = 0.3\%$) and C_v is 0.03.

Table 12: Results for porosity REV analysis of sample 1_34A.

	Volume (mm³)	Porosity (%)	Absolute Error (%)	Relative Error (%)	Mean	STD	C_v
Plug	21846	10.4%	-	-			
Q	13775	10.3%	0.03%	0.3%			
P1	6885	10.5%	0.12%	1.2%			
P2	6885	10.2%	0.18%	1.7%	10.3%	0.1%	0.011
Q1	3444	11.0%	0.58%	5.6%			
Q2	3444	10.0%	0.35%	3.4%			
Q3	3444	10.7%	0.28%	2.7%			
Q4	3444	9.9%	0.50%	4.8%	10.4%	0.3%	0.032
Q11	1722	11.2%	0.78%	7.5%			
Q12	1722	10.8%	0.38%	3.7%			
Q21	1722	8.7%	1.72%	16.6%			
Q22	1722	11.4%	1.02%	9.8%			
Q31	1722	10.4%	0.03%	0.3%			
Q32	1722	10.9%	0.53%	5.1%			
Q41	1722	9.7%	0.67%	6.5%			
Q42	1722	10.0%	0.33%	3.2%	10.4%	0.6%	0.061

The porosity was estimated to a total of 1 sample and 6 subsamples for the carbonate EB_1. The total volume of the slab was first analyzed, then, in the XY direction it was divided into other two squares, which were then, divided into other two new squares. The results for the porosity estimated for each subsample and sample are plotted as a function of sample volume in the Figure 36. From the 4 subsamples that presented a volume approximately 170 mm³, only one sample showed a variety higher than 10%. Therefore, considering a confidence percentage 99% percent, the subsamples above approximately 350 mm³ can be considered as REV for porosity for the Edwards Browns EB_1.

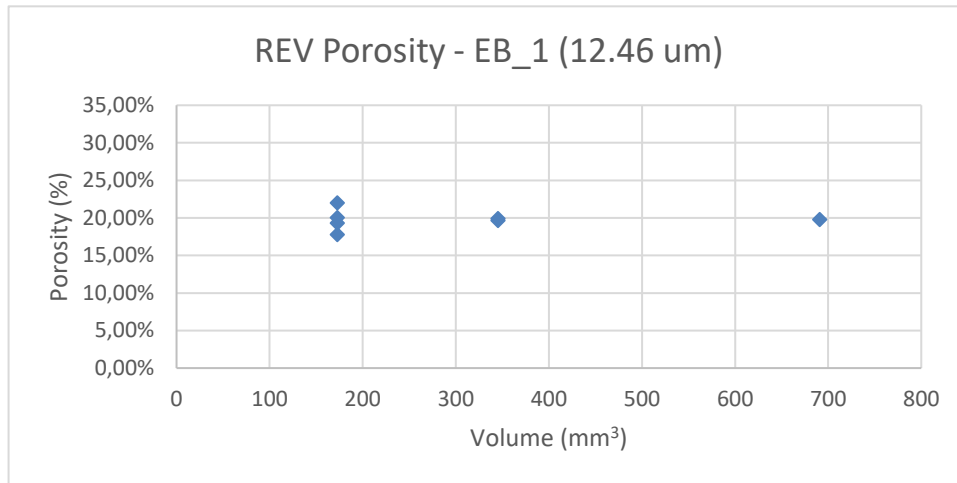


Figure 36: REV analysis for porosity of sample EB_1.

Table 13: Results for porosity REV analysis of sample EB_1.

	Volume (mm³)	Porosity (%)	Absolute Error (%)	Relative Error (%)	Mean	STD	C_v
Slab	691	19.8%					
P1	345	19.9%	0.13%	0.6%			
P2	345	19.7%	0.11%	0.6%	19.8%	0.1%	0.006
Q1	173	22.0%	2.24%	11.3%			
Q2	173	17.8%	1.99%	10.1%			
Q3	173	20.0%	0.24%	1.2%			
Q4	173	19.3%	0.47%	2.4%	19.8%	1.2%	0.061

The porosity was estimated to a total of 1 sample and 7 subsamples for the carbonate EB_3. The same methodology of division was applied to this sample. The results for the porosity estimated for each subsample and sample are plotted as a function of sample volume in the Figure 37. Due to the high heterogeneity, also represented by the number of shells found in the volume studied, this sample presented a large variety of porosity. Consequently, at the second degree of subsampling a value of 11.5% percentual error could be found. For this reason, it is recommended, with a confidence percentage of 93.5%, that volumes above approximately 6000 mm³ to be used for the study of porosity this sample.

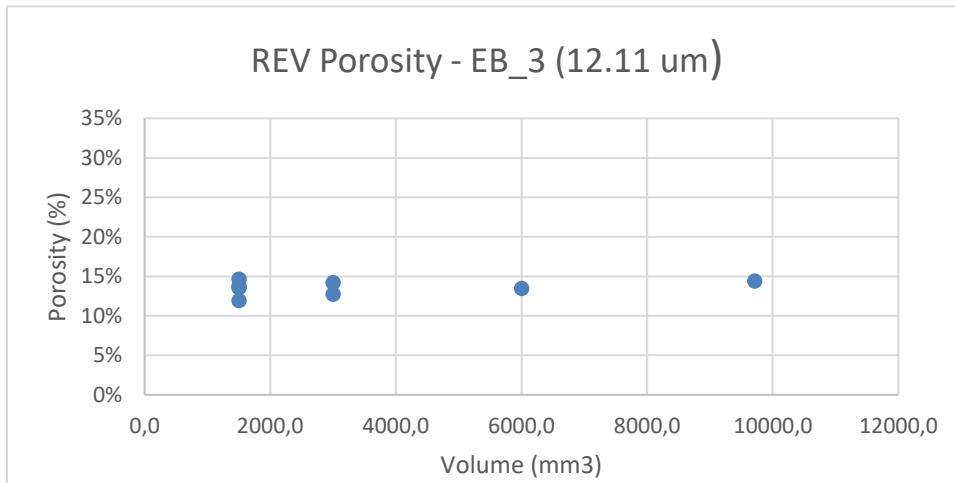


Figure 37: VER analysis for porosity of sample EB_3.

If the results are compared to the sample lithology sample, EB_1, the results for EB_3 present a large variety, the mean porosity of the first 4 samples is 13.7% and do not reflect the value for the entire sample. Additionally, the Cv values for the first group presents a larger value if compared to sample 1_34A and EB_1, which indicates a larger heterogeneity for this sample.

Table 14: Results for porosity REV analysis of sample EB_3.

	Volume (mm³)	Porosity (%)	Absolute Error (%)	Relative Error (%)	Mean	STD	Cv
Plug	9711	14.4%	-	-			
Q	6000	13.5%	0.93%	6.5%			
P1	3000	12.8%	1.66%	11.5%			
P2	3000	14.2%	0.20%	1.4%	13.7%	0.7%	0.052
Q1	1500	13.6%	0.84%	5.8%			
Q2	1500	11.9%	2.49%	17.3%			
Q3	1500	13.8%	0.63%	4.4%			
Q4	1500	14.6%	0.23%	1.6%	13.6%	0.8%	0.064

4.3.2 Permeability REV

Pore network modeling and fluid flow simulations for obtaining permeability were performed using PoreFlow to the same 1 sample and 15 subsamples volumes from the coquina 1_34A. The permeability calculated by PoreFlow considers only squared

volumes, therefore the permeability of the cylindrical plug sample was underestimated and was not presented at this work. The results are plotted in the Figure 38 against the sample volume. The results indicate an increase in permeability variation as the sample volume decrease. The results for the eight 1700 mm³ squares vary up to one order of magnitude above and below. Considering the variability of permeability as a log distribution, subsamples volumes above 6900 mm³ were found to be at the same order of magnitude from the lab experiments. However, only the volume of 13700 mm³ was able to represent the laboratory measured value for this sample, considering a maximum variation of 196 mD.

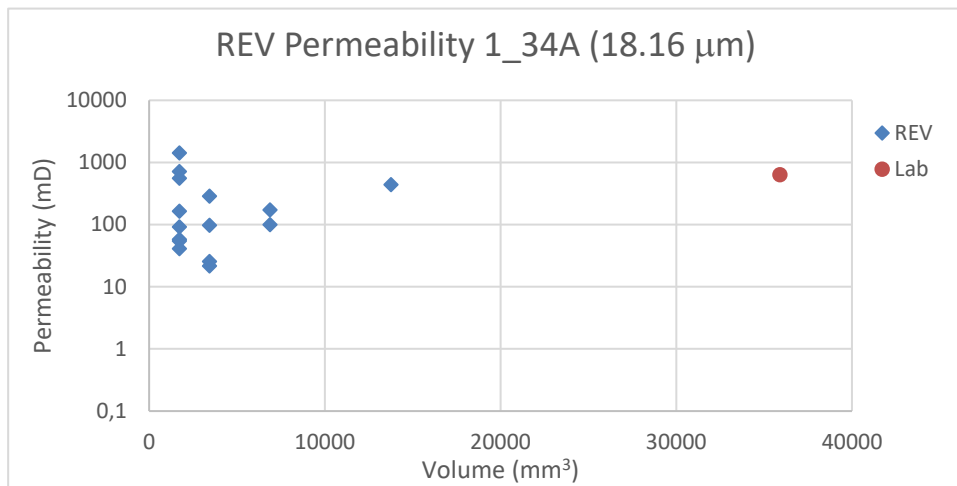


Figure 38: REV analysis for permeability of sample 1_34A.

The table below presents the statistics for these estimations as a function the logarithm at base 10 due to the log scale variability of permeability. Only the samples above 6887 mm³ present a relative error inferior to 25%. According to the classification of Corbett and Jensen (1997) all the measurements present $C_v < 0.5$, and therefore show a homogeneous behavior. Nonetheless, solely the samples volumes of 6887 mm³ and above present a higher accuracy and can be treated as REV. They present C_v of 0.13, while the smaller subsamples present a C_v of 0.24.

Table 15: Results for permeability REV analysis of sample 1_34A.

	Volume (mm³)	K (mD)	Absolute Error (%)	Relative Error (%)	Mean (log10)	STD (log10)	C_v
Q	13775	443.4					
P1	6885	100.5	64.5%	24.4%			
P2	6885	172.7	41.0%	15.5%	2.3	0.27	0.13
Q1	3444	97.5	65.8%	24.8%			
Q2	3444	25.5	124.0%	46.8%			
Q3	3444	286.8	18.9%	7.1%			
Q4	3444	21.8	130.8%	49.4%	2.0	0.46	0.24
Q11	1722	1426.6	50.8%	19.2%			
Q12	1722	165.0	42.9%	16.2%			
Q21	1722	54.7	90.9%	34.3%			
Q22	1722	92.7	68.0%	25.7%			
Q31	1722	716.7	20.9%	7.9%			
Q32	1722	556.3	9.9%	3.7%			
Q41	1722	41.2	103.2%	39.0%			
Q42	1722	58.1	88.3%	33.3%	2.1	0.52	0.24

The pore network models and fluid flow simulations, considering the harmonic average for the throat radius, were performed for the 1 sample and 6 subsamples of the slab EB_1. The results for permeability are plotted against sample volume in the Figure 39. The plot indicates an increase in permeability variation as the sample volume decrease, however, even for the largest volume the result is one order of magnitude higher than the value measured in laboratory. Therefore, the slab sample of the Edwards Brown carbonate, EB_1, cannot be considered as REV for permeability.

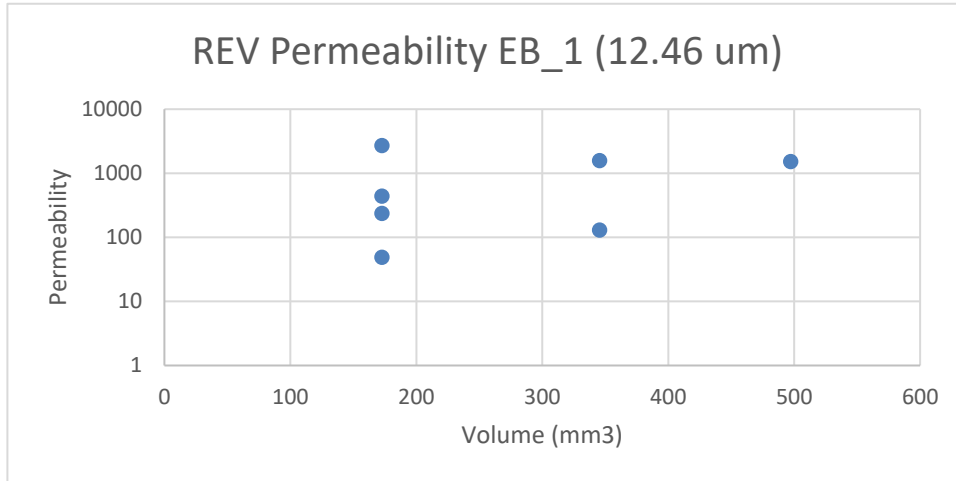


Figure 39: REV analysis for permeability of sample EB_1.

If the sample volumes are compared to the one studied in the sample 1_34A, we find that, even the largest sample available was smaller than the smaller subsample from the coquina. Nonetheless, this subsample presented a homogeneous behavior within its volume, that even considering all samples the coefficient of variation was 0.234.

Table 16: Results for permeability REV analysis of sample EB_1.

	Volume (mm³)	K (mD)	Absolute Error (%)	Relative Error (%)	Mean (log10)	STD (log10)	C_v
Slab	691	1627.2					
P1	345	1575	0.01416	0.00441			
P2	345	130.97	1.09427	0.34074	2.84	0.51	0.20
Q1	173	2717.4	0.22271	0.06935			
Q2	173	442.38	0.56565	0.17613			
Q3	173	49.112	1.52025	0.47339			
Q4	173	236.63	0.83737	0.26075	2.66	0.60	0.234

Pore network modeling and fluid flow simulations for the obtaining permeability were performed for 1 sample and 6 subsamples volumes from the plug EB_3. The results are plotted in the Figure 40 against the sample volume. The results indicate an increase in permeability variation as the sample volume decrease and also present a decrease of permeability. The results for the volumes below 3000 mm³ vary up from the same order of magnitude of the lab measurement up to one order below. The only samples that

presented results at the same order of magnitude from the lab measurement is the volume above 6000 mm³. Therefore, only measurements above this volume can be considered to present higher confidence, considering a maximum variation of 92 mD from the lab measurement. Because this sample presented a high variability for porosity it is safer to consider the minimum volume as REV being the “Q” subsample.

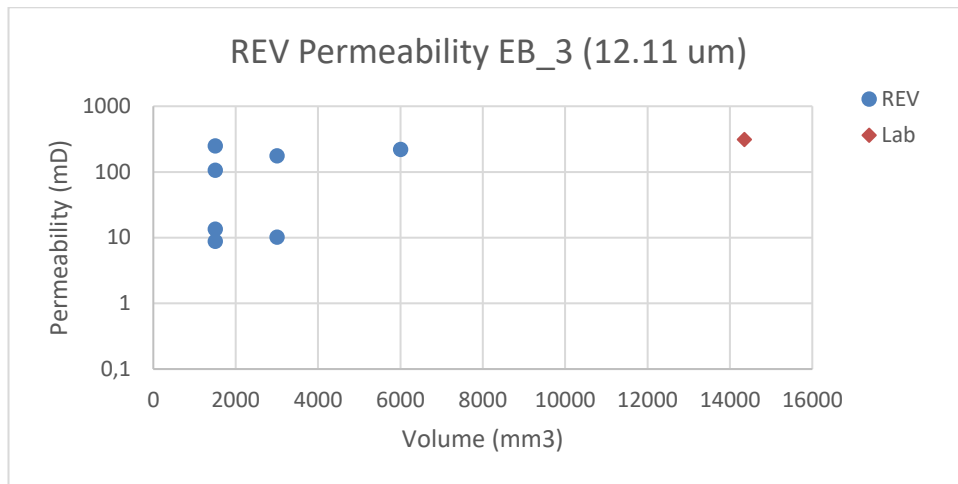


Figure 40: REV analysis for permeability of sample EB_3.

The variation indices are presented in the table below, it is possible to observe that even the largest values 3000 mm present a relative error of 57%. This sample presents the largest coefficient of variability, and according to Corbett and Jensen (1992) classification it can be considered as heterogenous sample.

Table 17: Results for permeability REV analysis of sample EB_2.

	Volume (mm3)	K (mD)	Absolute Error (%)	Relative Error (%)	Mean (log10)	STD (log10)	Cv
Q	6000	222.0	-	-			
P1	3000	176.6	9.9%	4.2%	136.2	91.06	0.50
P2	3000	10.2	133.9%	57.1%			
Q1	1500	106.5	31.9%	13.6%			
Q2	1500	248.9	5.0%	2.1%	112.4	96.93	0.65
Q3	1500	13.5	121.7%	51.8%			
Q4	1500	8.9	139.9%	59.6%			

4.4 PORE NETWORK SIMULATION

Considering the REV analysis performed in the last section, where it was evaluated the porosity and permeability variability of the samples, the “Q” samples, which were the largest representative volume from the samples’ volumes analyzed, were selected for synthetic pore network modeling.

4.4.1 Micro-CT Pore Network Statistics

The data from the micro-CT PNM were statistically analyzed regarding their pore size distribution, pore-throat and length distribution and mean coordination number.

4.4.1.1 Coquina Sample 1_34A – 18 microns

The data regarding pore radius of the PNM from the “Q” sample from the plug 1_34A was first analyzed. The log of the pores radius was histogram plotted and a gaussian fitting was applied to de data (Figure 41a). A relevant information from the histogram plot is that, the first bar represents the minimum pore radius identifiable by this image resolution, which is $9\mu\text{m}$. There is a data cumulative is this bar because it represents all the pores that fitted in one pixel, but also the smaller pores that could not be well characterized by this image resolution and were classified as pore according to the threshold selected. This peak was filtered from the gaussian fit to not induce errors. The second plot show the cumulative distribution of the gaussian fit (Figure 41b). The mean value for the gaussian fit is 4.2 and the standard deviation (STD) is 0.66.

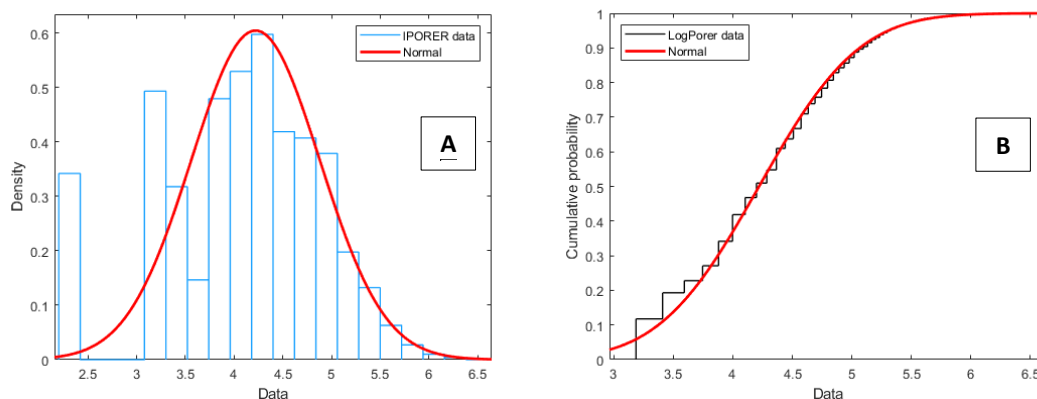


Figure 41: a) Pore size radius histogram and gaussian fit of sample 1_34A; b) Cumulative distribution of the fit.

The data regarding throat radius, considering the arithmetic average, of the PNM from the “Q” sample from the plug 1_34A was also analyzed. The log of the throat radius was histogram plotted and a gaussian fitting was applied to de data (Figure 42a). Similar to the pore radius histogram, the first bar presented a cumulative result. In this situation it was not filtered from the gaussian fit as it did not impact the results. The second plot shows the cumulative distribution of the gaussian fit (Figure 42b). The mean value for the gaussian fit is 4.14 and the STD is 0.68.

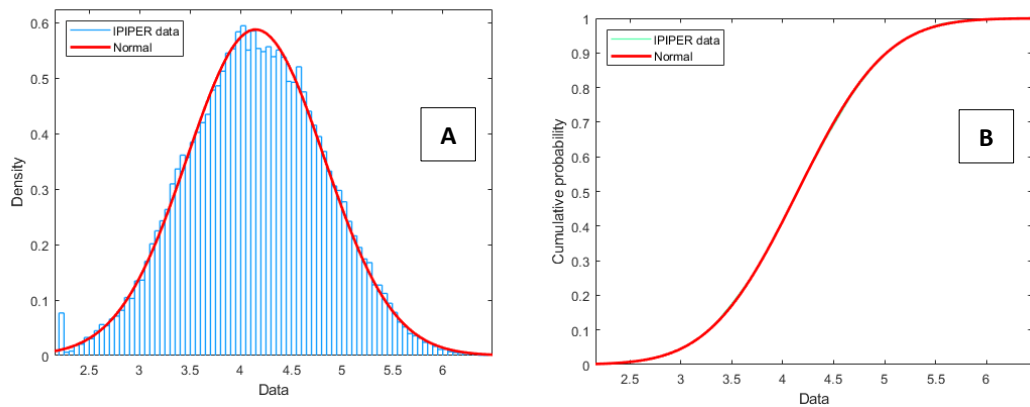


Figure 42: a) Pore throat radius histogram and gaussian fit of sample 1_34A; b) Cumulative distribution of the fit.

Equivalent analysis was performed for the throats length distribution and is presented in the plot below. The mean value for the gaussian fit for this variable is 5.51 and the STD is 0.67.

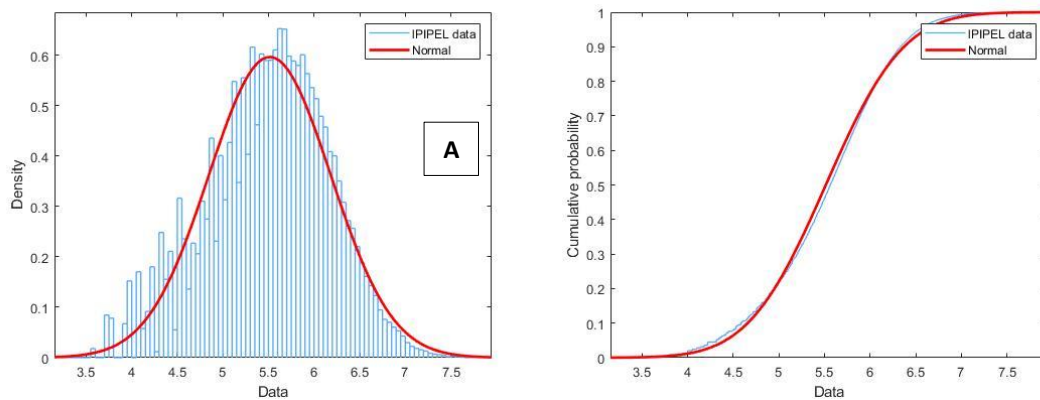


Figure 43: a) Throat length histogram and gaussian fit of sample 1_34A; b) Cumulative distribution of the fit.

Finally, the coordination number was histogram plotted (Figure 44). This data presented a large variability, what is expected for carbonates. The arithmetic average for this sample was 2.4. The statistical data from this section were further applied to the generation of synthetic PNM.

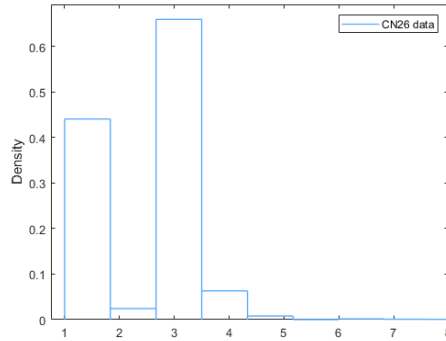


Figure 44: Coordination number histogram of sample 1_34A.

4.4.1.2 Edwards Brown Sample EB 3 – 12 microns

The data regarding data of the PNM from the “Q” sample from the plug EB_3 were analyzed similarly to the 1_34A sample. For this case, the model from the micro-CT images with resolution of 12 μ m was applied because they showed more representative results of the lab measurements. The log of the pores radius was also histogram plotted and a gaussian fitting was applied to de data (Figure 45a). The fitting was filtered in order to remove the noise from the first peak, which in this case represented pores radius of up to 6 μ m. The second plot show the cumulative distribution of the gaussian fit (Figure 45b). The mean value for the gaussian fit is 3.66 and the standard deviation (STD) is 0.6.

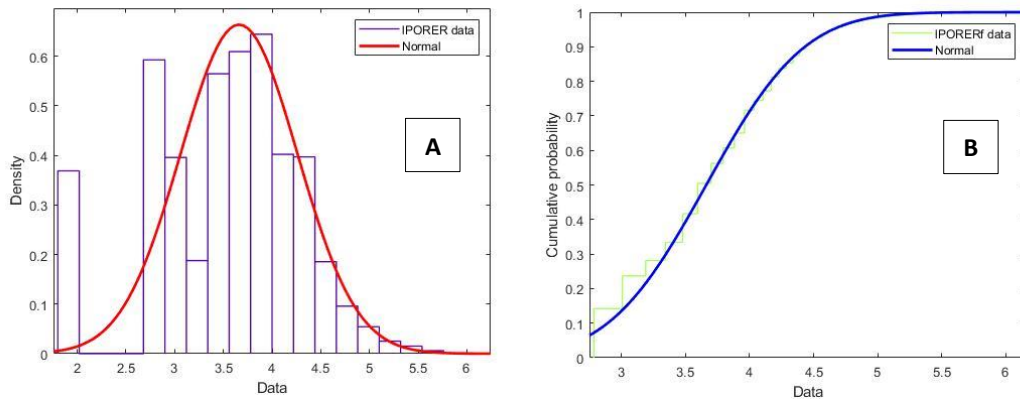


Figure 45: a) Pore size radius histogram and gaussian fit of sample EB_3; b) Cumulative distribution of the fit.

The data presented in the figures 46 and 47 were evaluated as described in the previous section. The mean value for the gaussian fit of throat radius is 3.51 and the STD is 0.62, while for throat length the mean is 4.9 and the STD is 0.61.

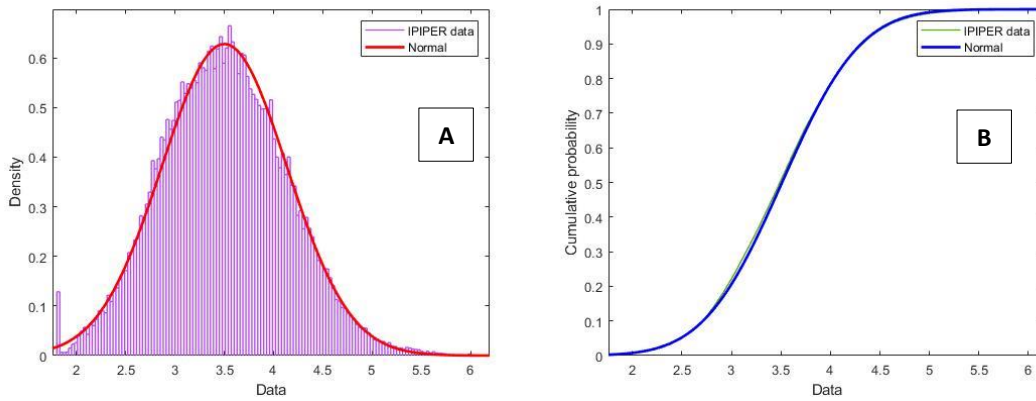


Figure 46: a) Pore throat radius histogram and gaussian fit of sample EB_3; b) Cumulative distribution of the fit.

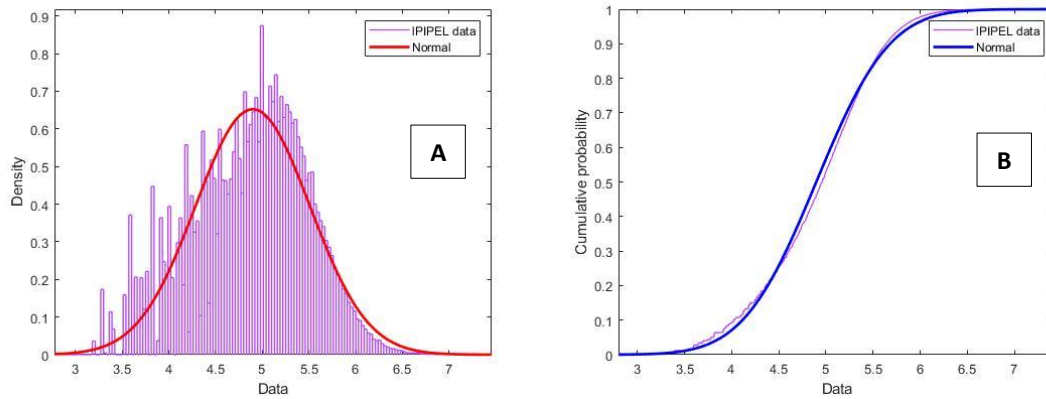


Figure 47: a) Throat length histogram and gaussian fit of sample EB_3; b) Cumulative distribution of the fit.

The mean coordination number calculated for EB_3 was 2.7. This data presents a large variability, but the highest frequency values range from 2 to 4.

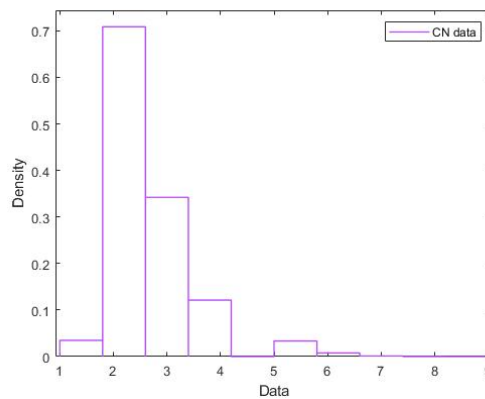


Figure 48: Coordination number histogram of sample EB_3.

4.4.2 Comparison of Micro-CT and Synthetic Pore Network Models

4.4.2.1 Coquina 1_34A – 18 μ m – Original Network Inputs

The results for the synthetic network representing the ‘Q’ volume from the coquina sample 1_34A with 18.16 μ m of resolution are discussed in the following topics:

- i. Characteristic length (Ncont): considering the lattice structure of our synthetic model, a challenge faced was regarding the fixed distance between each node center for (i,j,k) directions. The random nature of rocks networks and the carbonate rock heterogeneity may result that, the distance between each pore in the network presents a large variability. Additionally,

reproducing this characteristic in a lattice network may not be possible due to the different nature of their structures. For the coquina 1_34A, we established a Ncont of 387.6 μ m by modeling the synthetic PNM focused on meeting the average length of the distance between the pore in the micro-CT network, which is approximately 306 micrometers.

- ii. Coordination number: the coordination number was observed to be the variable that would most impact the results. It controlled the overall connectivity of the network, which directly impacts the permeability and the ratio of number of pores to number of throats. Additionally, it will impact the porosity in two manners: 1) reducing the porosity related to the throats and, 2) as increasing is the probability of the connections to the excluded is the number of pores with no connections or dead-end, which are then excluded from the network and will also impact the porosity. The probability of a connection to be excluded was set to 0.9356, in a scale from 0 to 1, for all 13 directions. It is important to notice that all directions presented the same probability, therefore we would not generate any artificial anisotropy effect on the model. To conclude, the final coordination number modeled was 2.41, and is a good agreement with the micro-CT PNM, presenting only a 1% of relative error.
- iii. The porosity and permeability results from both micro-CT and synthetic network were very similar, presented a relative error of 3.7 and 1% respectively. This result proposes that the topology aspects of the pore space network could be represented by the lattice network for this rock.
- iv. The number of pores and throats presented consistent results with error of 1.2% for number of pores and approximately 0% for number of throats.
- v. The total volume of the sample presented a minor difference of 1.4%.
- vi. Mean pore and throat radius were also consistent with a maximum error of 0.2%.
- vii. The number of inlet and outlet pores varies from the original and synthetic PNM. This effect happens because in the synthetic the surface of the sample is very flat, as it follows a lattice structure, therefore both inlet and outlet number of pores are similar. On the other hand, in the original rock network, this parameter is selected considering the pores contained in the 2% of the

total sample length at the top and bottom of the sample. It may change if we select 3 or 1% to be inlet, but it is dependent of the randomness of the rock pore network.

- viii. Visually analyzing both micro-CT and synthetic PNM it is possible to observe that first, the synthetic network is better distributed all over the sample volume. Second, in the synthetic network the pores are placed following a random distribution while in the micro-CT network they present a certain continuity, where it is possible to observe an agglomerate of large pores. Both phenomena result that in the micro-CT PNM there are channels of preference for the fluid flow, while in the synthetic the flow is distributed all over the space.

Table 18: Parameters statistics for micro-CT and synthetic (original network inputs) PNM models of sample EB_3.

	Micro-CT PNM	Synthetic PNM	Relative Error (%)
Porosity (%)	9.3%	9.0%	3.7%
Permeability (mD)	443.4	417.54	1.0%
No Pores	69527	68705	1.2%
No Inlet Pores	929	731	21.3%
No Outlet Pores	548	772	40.9%
No Throats	82963	82942	0.0%
Coordination number	2.4	2.4	0.0%
Volume (mm ³)	13755	13559	1.4%
Mean Pore Radius (μm)	79.1	79.2	0.2%
Mean Throat Radius (μm)	79.4	79.4	0.0%
Mean Throat Length (μm)	306.3	306.4	0.0%
N_{cont} (μm)	385.4	385.6	0.0%

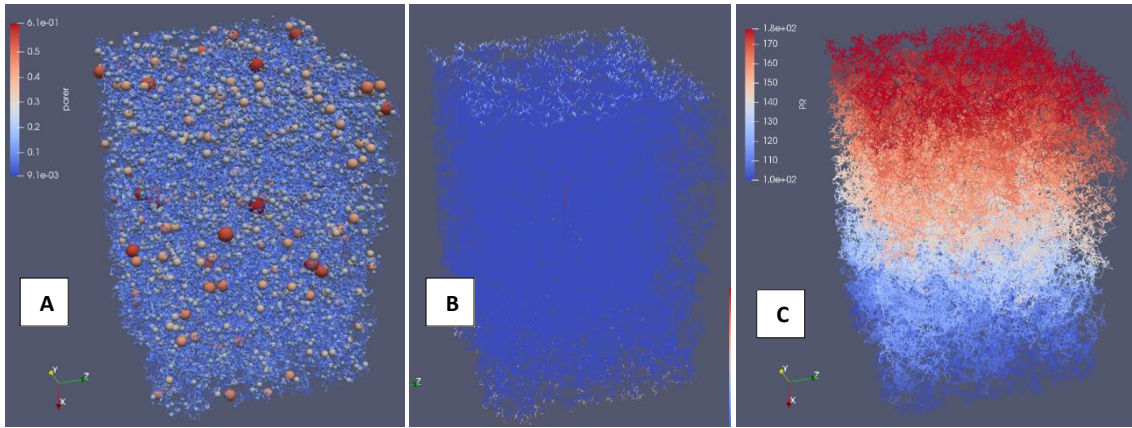


Figure 49: Sample 1_34A synthetic PNM a) Pore sizes; b) Inlet and outlet zones for fluid flow; and c) Final pressure gradient of fluid flow.

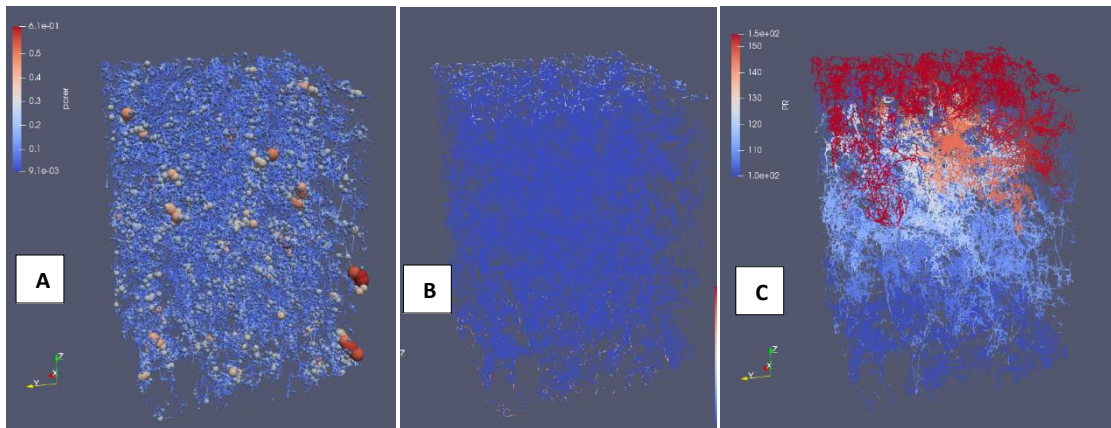


Figure 50: Sample 1_34A micro-CT PNM a) Pore sizes; b) Inlet and outlet zones for fluid flow; and c) Final pressure gradient of fluid flow.

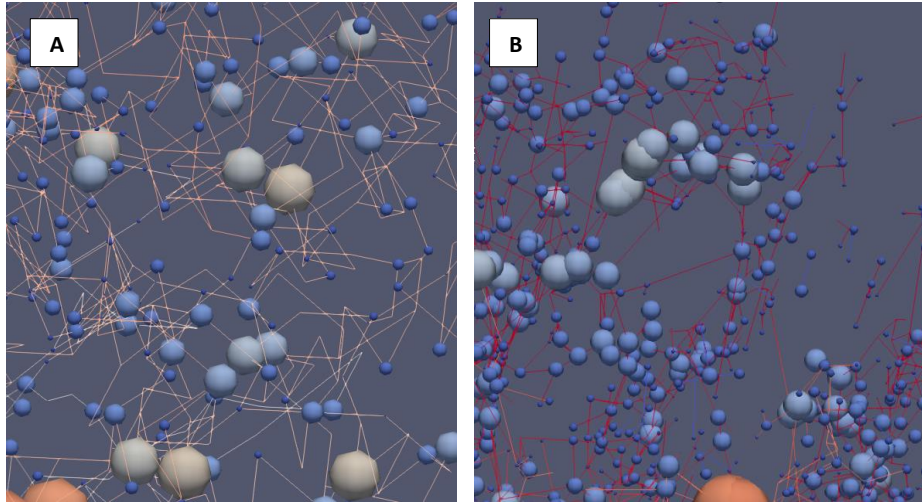


Figure 51: Pore networks and connections of a) 1_34A synthetic network; and b) 1_34A micro-CT network.

4.4.2.2 Coquina 1_34A – 18 μ m – PDF Distribution Inputs

A second approach was implemented for the generation of the synthetic PNMs. The normal probability distribution functions analyzed in the section 4.2.33 were applied to the generation of a synthetic PNM. The parameters encountered in the fitting of the normal distribution were used to create new arrays of inputs for the generation of synthetic PNM. As expected, if the normal distribution were representative of the real data, the results for this network should be similar to the ones obtained using the original PNM data.

Additionally, we ran sensitivity tests to evaluate the effect of generating a PNM with the mean average value for selected properties, while keeping the others as the original micro-CT PNM. The distributions considered for this study were pore radius, throat size and length and average coordination number. The results for the synthetic network are discussed in the following topics:

- i. Characteristic length (Ncont): the PNM generated from the statistics information show a slight increase compared to the micro-CT PNM, resulting in a total of 2.7% of relative error.
- ii. Coordination Number: this parameter was kept constant from section 4.4.1.
- iii. The porosity and permeability errors from section 4.4.1 changed from 3.7% and 1%, to 12.6% and 0.6%, respectively. Therefore, the statistical data shows a good correlation with the analyzed with micro-CT.

- iv. The parameters of number of inlet and outlet pores, number of pores, number of throats, sample volume maintained the same values.
- v. The mean values for pore radius, throat radius and throat length presented a error of 7.1%, 0.3% and 1.6%, which were larger than section 4.4.1 but were able to present fidelity to original micro-CT sizes distribution.

Table 19: Parameters statistics for micro-CT and synthetic (statistical distributions) PNM models of sample 1_34A.

	Micro-CT PNM	Synthetic PNM (PORER, PIPER, PIPEL)	Relative Error (%)
Porosity (%)	9.3%	10.5%	12.6%
Permeability (mD)	443.4	426.81	0.6%
No Pores	69527	68705	1.2%
No Inlet Pores	929	731	21.3%
No Outlet Pores	548	772	40.9%
No Throats	82963	82942	0.0%
Coordination number	2.4	2.4	1.0%
Volume (mm ³)	13755	13559	1.4%
Mean Pore Radius (um)	79.1	84.7	7.1%
Mean Throat Radius (um)	79.4	79.7	0.3%
Mean Throat Length (um)	306.3	311.3	1.6%
Nc (um)	385.6	396.0	2.7%

Considering the sensitivity tests ran in the synthetic PNM with constant mean properties for i) pore radius and ii) throat radius the following aspects were observed:

- i. The mean pore radius did not affect the results for permeability, which were kept at the constant value of 417.54 mD, showing that the permeability is majorly controlled by the throats. However, the error between the micro-CT original and synthetic networks from section 4.4.1 increased from 3.7% to 21.5% using this approach.
- ii. On the other hand, applying a constant throat radius for the network, while keeping the other PNM parameters equal to the synthetic PNM from section 4.4.1 generated a catastrophic impact on the permeability results. It shows the relevance of the throats on fluid flow, and the importance of representing the variability encountered in the distribution of the throat radius.

4.4.2.3 Limestone EB_3 – 12 μ m – Original Network Inputs

The results for the synthetic network representing the ‘Q’ volume from the limestone sample EB_3 with 12.11 μ m of resolution are discussed in the following topics:

- i. Characteristic length (Ncont): as discussed in the previous section, reproducing the characteristic length was a challenge considering the lattice structure of our synthetic model. For EB_3 the value of Ncont established was 204.5 μ m, distance smaller than the sample 1_34A, what suggests a higher porosity and a higher density of pores per rock volume.
- ii. Coordination number: for this sample, the probability of a connection to be excluded was set to 0.9259, in a scale from 0 to 1, for all 13 directions. To conclude, the final coordination number modeled was 2.6 while the original micro-CT PNM presented an average of 2.7.
- iii. The porosity and permeability results from both micro-CT and synthetic network presented an acceptable error. They presented a relative error of 5.3 and 10.5% respectively. The larger difference from the micro-CT happens due to its heterogeneity behavior. An important fact to note is that, at the center of the plug there is located a large shell, that presents almost 0% porosity. This shell generates this large heterogeneity and also impacts on the quality of input layer for fluid flow in the simulation. If observed in the figure 53, in the original micro-CT the pressure gradient happens in preferential channels of flow. On the other side, the standard synthetic PNMs modeled in PoreFlow do not reproduce this behavior. It uniformly distributes the PNM components in the space in order to get the same estimate. In this case, the standard modeling is unable to reproduce completely the heterogeneous aspects that impact the quality of such rock. This issue will be addressed in the next section.
- iv. The number of pores and throats presented consistent results with error of 0.6% for number of pores and approximately 6.5% for number of throats.
- v. The total volume of the sample presented a negligible relative error of 1.2%.
- vi. Mean pore and throat radius were also consistent with an error of 0.3 and 0.6% respectively.

- vii. The number of inlet and outlet pores varies from the original and synthetic PNM. First, this effect happens because in the synthetic the surface of the sample is very flat and follows a lattice structure, but specially for this model, the sample presents a high heterogeneity at the inlet region that could not be fully represented.

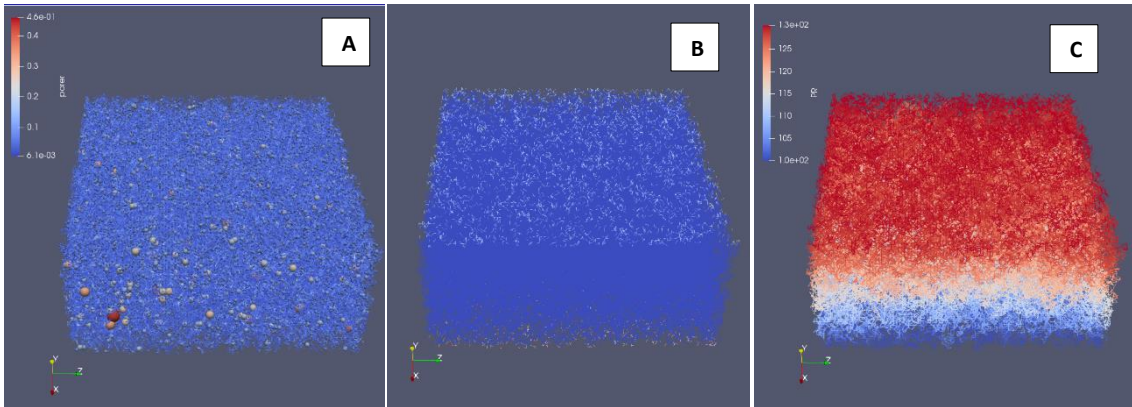


Figure 52: Sample EB_3 synthetic PNM a) Pore sizes; b) Inlet and outlet zones for fluid flow; and c) Final pressure gradient of fluid flow.

Visually analyzing micro-CT PNM it is possible to observe a high density of pores and throats that are concentrated in specific regions, while others do not present any of these PNM components. In the synthetic PNM, the density is smaller than the micro-CT network but it still dense and is well distributed.

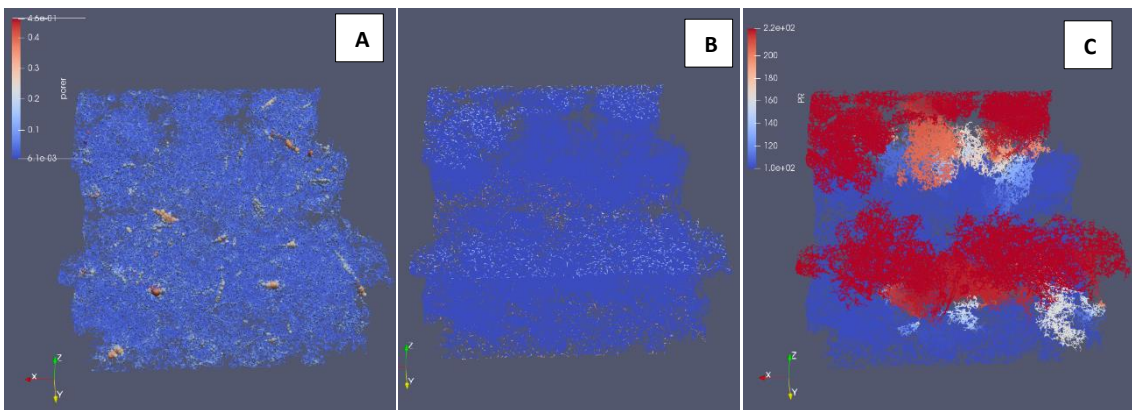


Figure 53: Sample EB_3 micro-CT PNM a) Pore sizes; b) Inlet and outlet zones for fluid flow; and c) Final pressure gradient of fluid flow.

Table 20: Parameters statistics for micro-CT and synthetic (original network inputs) PNM models of sample EB_3.

	Micro-CT PNM	Synthetic PNM	Relative Error (%)
Porosity (%)	9.7%	9.2%	5.3%
Permeability (mD)	221.43	390.59	10.5%
No Pores	192950	191761	0.6%
No Inlet Pores	1866	3556	90.6%
No Outlet Pores	3739	3593	3.9%
No Throats	261723	244624	6.5%
Coordination number	2.7	2.6	6.0%
Volume (mm ³)	6091.3	6020.5	1.2%
Mean Pore Radius (um)	43.7	43.8	0.3%
Mean Throat Radius (um)	40.8	41.1	0.6%
Mean Throat Length (um)	159.6	160.7	0.7%
Nc (um)	203.3	204.5	0.6%

With the objective to reproduce the damage on the connections caused by the presence of the shell in the rock sample, it was introduced a similar behavior in the synthetic network. We used the same model parameters from the previous synthetic PNM, but we modified the classification of the pores in the central region from inlet to regular pores. In this way, fluid flow from adjacent cells still may happen and will contribute to the overall permeability, but at least the PNM results can account for the reduced inlet region.

The following results were observed:

- i. There was a slightly increase in porosity that happened due to the added pores that were previously classified as “inlet” pores.
- ii. The total number of inlet pores present exactly the sample quantity as the micro-CT network.
- iii. Good results could be observed regarding permeability, there was a reduction from 390 mD from the regular synthetic network to 338 mD. This indicates that for some degrees of heterogeneity regular synthetic network may not be the best representative model, yet presents a good level of accuracy, but that adding heterogenous effects on the modelling may be important to better represent the pore space.

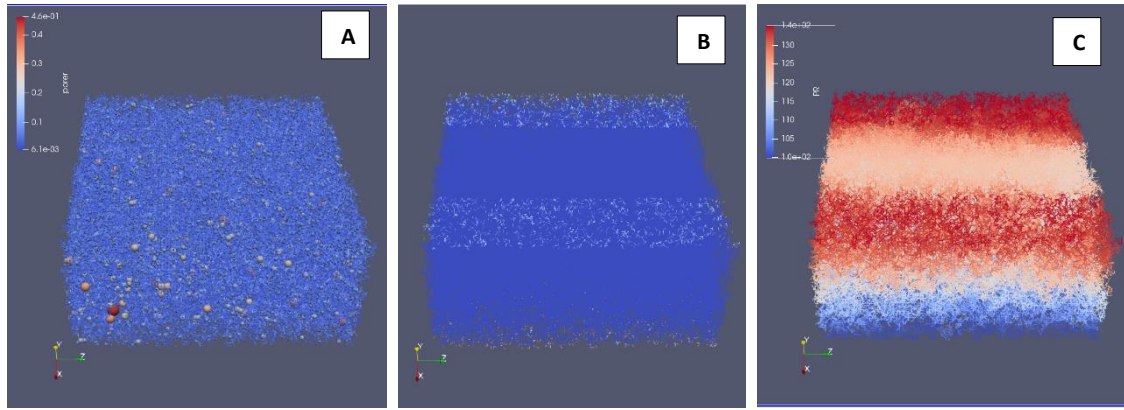


Figure 54: Sample EB_3 synthetic PNM with modified input zone a) Pore sizes; b) Inlet and outlet zones for fluid flow; and c) Final pressure gradient of fluid flow.

Table 21: Parameters statistics for micro-CT and synthetic (with modified input layer) PNM models of sample EB_3.

	Micro-CT PNM	Synthetic PNM (modified input layer)	Relative Error (%)
Porosity (%)	9.7%	9.6%	1.2%
Permeability (mD)	221.43	335.88	7.7%
No Pores	192950	191761	0.6%
No Inlet Pores	1866	1866	0.0%
No Outlet Pores	3739	3593	3.9%
No Throats	261723	244624	6.5%
Coordination number	2.7	2.6	6.0%
Volume (mm ³)	6091.3	6020.5	1.2%
Mean Pore Radius (um)	43.7	43.8	0.3%
Mean Throat Radius (um)	40.8	41.1	0.6%
Mean Throat Length (um)	159.6	160.7	0.7%
Nc (um)	203.3	204.5	0.6%

4.4.2.4 Limestone EB 3 – 12 μ m – PDF Distribution Inputs

The same approach from section 4.4.2 was implemented for the generation of the synthetic PNMs using the normal probability distribution functions analyzed in the section 4.2.33. We also ran sensitivity tests to evaluate the effects of constant mean averages for selected PNM parameters. The distributions considered for this study were pore radius, throat size and length and average coordination number. These PNMs were generated considering the standard synthetic PNM parameters from section 4.4.3,

therefore, we did not introduce the shell effect on the inlet region. The results for the synthetic network are discussed in the following topics:

- i. It was observed an increase in the error to represent the porosity from 5 to 10% in this case. This fact may indicate again about the heterogeneity of the sample, that impacts on the uniform distribution of pores. Although the mean pore radius of the distribution is larger than the mean pore radius of the micro-CT, it did not fully capture the heterogeneity of the data.
- ii. The permeability presented an increase of relative error from 10.5 to 12.1 %. The throat radius is a parameter that affects the permeability, and although the mean pore throat of the distribution is 0.8% smaller than the micro-CT PNM the results for this network were larger.
- iii. Additionally, the tests ran keeping one parameter at constant mean value, for example, all pores with same radius or all throats with the same radio showed similar results as the test from the coquina. Keeping the pores radius constant, did not affect the final value of permeability, showing the relevance of the throats for it, but it did decrease the porosity and generated an error of 38.5%. If compared to the coquina sample, this error is larger, which again is coherent with the conclusion about the high heterogeneity of this sample. For the tests keeping the pore radius at constant mean value, the results showed a relative error of 45.5% of permeability, also coherent with the conclusion about the importance of throat radius distribution to the final fluid flow.

Table 22: Parameters statistics for micro-CT and synthetic (statistical distributions) PNM models of sample EB_3.

	Micro-CT PNM	Synthetic PNM (PORER, PIPER, PIPEL)	Relative Error (%)
Porosity (%)	9.7%	8.6%	10.8%
Permeability (mD)	221.43	426.67	12.1%
No Pores	192950	191761	0.6%
No Inlet Pores	1866	3556	90.6%
No Outlet Pores	3739	3593	3.9%
No Throats	261723	244624	6.5%
Coordination number	2.7	2.6	6.0%
Volume (mm ³)	6091.3	6020.5	1.2%
Mean Pore Radius (um)	43.7	46.5	6.3%
Mean Throat Radius (um)	40.8	40.5	0.8%
Mean Throat Length (um)	159.6	161.4	1.1%
Nc (um)	43.7	240.0	449.1%

5 CONCLUSIONS

A comprehensive methodology was applied to integrate laboratory measurements and image processing to enable the simulation of three-dimensional digital rocks. Laboratory measurements such as porosity, permeability and NMT T2 curves were correlated to establish to develop digital models calibrated to the physical ones. Pore-size distribution curves were selected as the best approach to select threshold of segmentation for the digital rock models.

One of the main challenges faced in the simulation of these digital models were the heterogeneity of carbonates. This feature did not only translate in spatial heterogeneity but also affected the geometry of the pore space. To characterize the rock samples heterogeneity, a representative elementary volume study was conducted focused on the variation of porosity and permeability. Different behavior was found for the different types of carbonates studied, with special attention to the sample Edwards Brown that presented different coefficient of variation for different samples. The rock sample of Coquina, although a carbonate, presented a homogeneous behavior for permeability according to the Corbett and Jensen (1997) classification.

Moreover, to estimate the sample permeability and infer other pore geometry characteristics, we applied the methodology “maximal balls” for the discretization of the micro-CT images pore space and simulate pore network models. This methodology, which applies a representation of the pore space by simplified geometries, was able to transmit the complex pore space features affecting single-phase flow in the carbonates in this study, and therefore it provided approximate estimates of rock permeability.

Finally, the information obtained from statistics of the micro-CT pore network models were analyzed and were used as base for the generation of representative synthetic PNMs. The synthetic PNMs followed the work of Raouf and Hassanizadeh (2009) and presented a lattice structure, very different of the random nature of the PNM structure from rocks. Nonetheless, the synthetic PNMS were able generate similar PNMs parameters and be representative of coordination number and values of porosity and permeability. Furthermore, interesting challenges were faced when simulating the highly heterogeneous rock Edwards Brown, that presented sorted shells with very low presence of porosity in its volume.

5.1 FURTHER STUDIES

The methodology applied was very interesting and challenging due to the diverse behavior of the rocks. Interesting topics for improvement or for being deeply studied in future works include:

- i. Correlation of Mercury Injection Capillary Pressure Curves and NMR T_2 pore size curves to be applied in the generation and correlation to pore network models
- ii. Developments of rescaled PNM on sample volumes that cannot be imaged at higher resolution due to computational costs
- iii. Improvement and further studies to reproduce the heterogeneity encountered in carbonates by synthetic pore network models
- iv. Addition for multi-phase studies on both micro-CT and synthetic PNMs

6 BIBLIOGRAPHY

- AHMED, T. Reservoir Engineering Handbook. Elsevier, 3rd Edition, 2006.
- AL-KHARUSI, A.S., BLUNT, M.J. Network extraction from sandstone and carbonate pore space images. *J. Pet. Sci. Eng.* 56 (4), 219–231, 2007.
- ANDREETA, M. B. Topological study of reservoir rocks and acidification processes using complex networks methods. Doctoral dissertation, Universidade de São Paulo, São Paulo, 2017
- AVIZO. Reference Manual. Thermo Fisher Scientific. Version 9.5. January 2018
- BULTREYS, T., DE BOEVER, W., & CNUUDE, V. (2016). Imaging and image-based fluid transport modeling at the pore scale in geological materials: A practical introduction to the current state-of-the-art. *Earth-Science Reviews*, 155, 93-128.
- BLUNT, M. J., BIJELJIC, B., DONG, H., GHARBI, O., IGLAUER, S., MOSTAGHIMI, P., ... & PENTLAND, C. *Pore-scale imaging and modelling*. *Advances in Water Resources*, 51, 197-216, 2013.
- BLUNT, M.J. Flow in Porous Media — Pore-Network Models and Multiphase Flow. *Current Opinion in Colloid & Interface Science*, v. 6, pp. 197–207, 2001.
- BOYD, A. Private communication in August 2019.
- COATES, G. R., XIAO, L., & PRAMMER, M. G. *NMR logging: principles and applications*, Vol. 344, Haliburton Energy Services, Houston, 1999.
- CORBETT, P.W. M. Integration of Static and Dynamic Models. *Petroleum Geoen지니어ing. SEG/EAGE Distinguished Instructor Series*, v. 12, pp. 100–190, 2009.
- CORBETT, P.W.M., ANGGRAENI, S., BOWDEN, D. The Use of The Probe Permeameter In Carbonates-Addressing the Problems of Permeability Support and Stationarity. *Log Anal.*, v. 40 (5), pp.316–326, 1999.

- CORBETT, P.W.M., JENSEN, J. L. Variation of Reservoir Statistics According to sample spacing and measurement type for some intervals in the Lower Bent Group. *Log Analysts*, v. 40 (5), pp. 316-326, 1997.
- CNUDDE, V., & BOONE, M. N. High-resolution X-ray computed tomography in geosciences: A review of the current technology and applications. *Earth-Science Reviews*, 123, 1-17, 2013.
- DE VRIES, E. T., RAOOF, A., VAN GENUCHTEN, M. T. Multiscale modelling of dual-porosity porous media; a computational pore-scale study for flow and solute transport. *Advances in Water Resources*, v. 105, pp. 81-95, 2017.
- FERREIRA, F.V, STUKAN, M., LIANG, L., SOUZA, A., VENKATARAMANAN, L., BELETSKAYA, A., DIAS, D., DANTAS DA SILVA, M. New Model for Wettability Change with Depth in Mixed-Wet Complex Carbonates. *Society of Petroleum Engineers*, 2018. doi:10.2118/192758-MS
- FERREIRA, F.C., BOOTH, R., OLIVEIRA, R., BOYD, A., SPE, SCHLUMBERGER, BIZE-FOREST, N., AND WAHANIK, H. Truncated Multi-Gaussian Pore-Throat-Size Decomposition and a New Universal J-Function for Rock Characterization of Complex Carbonate Reservoirs. *Offshore Technology Conference Brazil*, 2015.
- GODOY, W., PONTEDEIRO, E. M., HOERLLE, F., RAOOF, A., GENUCHTEN, M. T., SANTIAGO, J. COUTO, P. Computational and experimental pore-scale studies of a carbonate rock sample. *J. Hydrol. Hydromech.*, 67, 2019, 4.
- HOERLLE, F., SILVA, E., RIOS, SILVA, W., G., PONTEDEIRO, E.M., LIMA, M. C. O., CORBETT, P., ALVES. J., COUTO, P. Nuclear Magnetic Resonance to Characterize the Pore System of Coquinas from Morro do Chaves Formation, Sergipe-Alagoas Basin, Brazil. *Revista Brasileira de Geofísica*, v. 36(3), pp. 1-8, 2018.
- HOERLLE, F., SILVA, W., RIOS, E., SILVEIRA, T., COUTO, P. ALVES. J. LIMA, M., CORBETT, P. Evaluation of Segmentation Procedures Using X-Ray

- Computed Microtomography Images of Coquinas from Morro Do Chaves Formation – Ne Brazil. Cilamce 2017, Florianopolis, Brazil, 2017.
- HUANG, D. D., HONAPOUR, M. M., AL-RUSSAINY, R. An Improved Model for Relative Permeability and Capillary Pressure Incorporating Wettability. 1997 SCA International Symposium, Canadá, 1997.
- HURLEY, N. F., ZHAO, W, ZHANG, T. Multiscale Workflow for Reservoir Simulation. SPWLA 53rd Annual Logging Symposium, June 16-20, 2012.
- HU, BIN & LANGSHOLT, MORTEN & LIU, LAN & ANDERSSON, PETER & LAWRENCE, CHRIS. (2014). Flow structure and phase distribution in stratified and slug flows measured by X-ray tomography. *International Journal of Multiphase Flow*. 67. 10.1016/j.ijmultiphaseflow.2014.06.011.
- KENYON, W. E. Petrophysical principles of applications of NMR logging. *The Log Analyst*, 38(02), 1997.
- KENNEDY, M. Developments in Petroleum Science. Practical petrophysics, Vol. 62, Elsevier, 2015.
- KHALILI, A. D., ARNS, C. H., ARNS, J. Y., HUSSAIN, F., CINAR, Y., PINCZEWSKI, W. V., ... & FUNK, J. Permeability upscaling for carbonates from the pore-scale using multi-scale Xray-CT images. In SPE/EAGE European Unconventional Resources Conference & Exhibition-From Potential to Production, 2012. doi:10.2118/152640-MS
- KUROTORIA, T., ZAHASKY, C., BENSON, S. M., PINI, R. Three-Dimensional Imaging of Solute Transport in Reservoir Rocks by Positron Emission Tomography. 14th International Conference on Greenhouse Gas Control Technologies, GHGT-14, Australia, 2018.
- KURY, F. Unlocking the Opportunities in the Brazilian Oil Industry. National Agency for Petroleum, Natural Gas and Biofuels (ANP) presentation, 2019.
- LUCIA, F. J. Carbonate reservoir characterization: An integrated approach. Springer Science & Business Media, 2007.

- LUNA J, PEROSI F.A, DOS SANTOS RIBEIRO M.G, SOUZA A, BOYDA A, DE ALMEIDA L.F.B. & CORBETT P.W.M. Petrophysical Rock Typing of Coquinas from the Morro do Chaves Formation, Sergipe-Alagoas, 2016. Basin (Northeast Brazil). *Revista Brasileira de Geofísica*, 34(4): 509–521, 2016.
- SCHLUMBERGER. (2018). *Carbonate Reservoirs*. Available in https://www.slb.com/services/technical_challenges/carbonates.aspx. Visited in August 6, 2018.
- MATADAMAS, J., ROMAN, G., ROJAS, F. CASTRO, M. A., CORERO, S., AGUILAR, M. Pore Network Simulation via Monte Carlo Algorithms on GPUs. *IEEE LATIN AMERICA TRANSACTIONS*, v. 12, n. 3, May 2014.
- OKABE, H., BLUNT, M. Pore space reconstruction using multiple-point statistics. *Journal of Petroleum Science and Engineering*, v. 46, pp.121–137, 2005.
- RAOOF, A., NICK, H.M., HASSANIZADEH, S.M., SPIERS, C.J. PoreFlow: a complex pore-network model for simulation of reactive transport in variably saturated porous media. *Comp. Geosciences*, v. 61, pp. 160–174. <http://dx.doi.org/10.1016/j.cageo.2013.08.005>., 2013
- RAOOF, A., HASSANIZADEH, S. M. A new method for generating pore-network models of porous media. *Transport in Porous Media*, v 81(3), pp. 391–407, 2009.
- SOUZA, A. Private communication in October 2018.
- SOUZA, A. A. D. Estudo de propriedades petrofísicas de rochas sedimentares por Ressonância Magnética Nuclear. Doctoral dissertation, Universidade de São Paulo, São Paulo, 2012.
- SOUZA, A., CARNEIRO, G., BOYD, A., HURLIMANN, M., TREVIZAN, W., COUTINHO, B., MACHADO, V., BAGUEIRA, R. Improving Lab Nmr Petrophysical estimations By Incorporating the Surface Relaxivity Parameter. International Symposium of the Society of Core Analysts held in Snowmass, Colorado, USA, 21-26 August 2016

- TIAB, D., & DONALDSON, E. C. *Petrophysics: theory and practice of measuring reservoir rock and fluid transport properties*. Gulf professional publishing, 2015.
- VIK. B, BASTESEN, E., SKAUGE, A. Evaluation of Representative Elementary Volume for A Vuggy Carbonate Rock—Part: Porosity, Permeability, And Dispersivity. *Journal of Petroleum Science and Engineering*, v. 112, pp. 36–47, 2013.
- WESTPHAL, H., SURHOLT, I., KIESL, C., THERN, H. F., & KRUSPE, T. NMR measurements in carbonate rocks: Problems and an approach to a solution. *Pure and Applied Geophysics*, 162(3), 549-570, 2005.
- XIONG, Q., BAYCHEV, T. G., JIVKOV, A. P. Review of Pore Network Modelling of Porous Media: Experimental Characterizations, Network Constructions and Applications to Reactive Transport. *Journal of Contaminant Hydrology*, v. 192, pp. 101-117, 2016.
- YOUNG, X., YANG, X., MEHMANI, Y., PERKINS, W., PASQUALI, A., SCHÖNHERR, M., KIMD, K., PEREGO, M., PARKS, M., TRASKE, N. BALHOFF, M., GEIER M., KRAFCZYKC, M., LUOG, L., TARTAKOVSKYA, A., SCHEIBEA, T.. Intercomparison of 3D pore-scale flow and solute transport simulation methods. *Advances in Water Resources*, v. 95, pp. 176-189, 2016.
- ZHANG, T. MPS-Driven Digital Rock Modeling and Upscaling. *Mathematical Geosciences*, v. 47, pp. 937-954, 2015.